

INFORMATION TO USERS

This manuscript has been reproduced from the microfilm master. UMI films the text directly from the original or copy submitted. Thus, some thesis and dissertation copies are in typewriter face, while others may be from any type of computer printer.

The quality of this reproduction is dependent upon the quality of the copy submitted. Broken or indistinct print, colored or poor quality illustrations and photographs, print bleedthrough, substandard margins, and improper alignment can adversely affect reproduction.

In the unlikely event that the author did not send UMI a complete manuscript and there are missing pages, these will be noted. Also, if unauthorized copyright material had to be removed, a note will indicate the deletion.

Oversize materials (e.g., maps, drawings, charts) are reproduced by sectioning the original, beginning at the upper left-hand corner and continuing from left to right in equal sections with small overlaps.

Photographs included in the original manuscript have been reproduced xerographically in this copy. Higher quality 6" x 9" black and white photographic prints are available for any photographs or illustrations appearing in this copy for an additional charge. Contact UMI directly to order.

**Bell & Howell Information and Learning
300 North Zeeb Road, Ann Arbor, MI 48106-1346 USA
800-521-0600**

UMI[®]

**Quantitative Analysis of Metabolic Breast Images from Positron Emission Mammography
(PEM)**

**Marianne Aznar
Medical Physics Unit
McGill University, Montreal**

May, 1999

**A thesis submitted to the Faculty of Graduate Studies and Research in partial fulfillment of the
requirements of the degree of Master of Science**



National Library
of Canada

Acquisitions and
Bibliographic Services

395 Wellington Street
Ottawa ON K1A 0N4
Canada

Bibliothèque nationale
du Canada

Acquisitions et
services bibliographiques

395, rue Wellington
Ottawa ON K1A 0N4
Canada

Your file *Votre référence*

Our file *Notre référence*

The author has granted a non-exclusive licence allowing the National Library of Canada to reproduce, loan, distribute or sell copies of this thesis in microform, paper or electronic formats.

The author retains ownership of the copyright in this thesis. Neither the thesis nor substantial extracts from it may be printed or otherwise reproduced without the author's permission.

L'auteur a accordé une licence non exclusive permettant à la Bibliothèque nationale du Canada de reproduire, prêter, distribuer ou vendre des copies de cette thèse sous la forme de microfiche/film, de reproduction sur papier ou sur format électronique.

L'auteur conserve la propriété du droit d'auteur qui protège cette thèse. Ni la thèse ni des extraits substantiels de celle-ci ne doivent être imprimés ou autrement reproduits sans son autorisation.

0-612-50714-9

Canada

ABSTRACT

X-ray mammography cannot always distinguish between benign and malignant breast lesions. This leads to unnecessary biopsies, costs, and stress for the patient. Positron Emission Mammography (PEM) provides images of increased glucose metabolism in malignant tumours compared with healthy tissue. After injection of a radioactively-labelled glucose analog, cancerous tumours appear as bright spots on the breast image.

Quantitative analysis of PEM images consists in comparing the amount of activity absorbed in both breasts of a patient. Based on ROC analysis of 15 subjects, an asymmetry of 10% in the number of counts detected from each breast was taken as a sign of cancer. The application of the count asymmetry method seems to result in a 22% improvement of PEM accuracy (from 64% to 86%). It is particularly useful for the detection of big or diffuse tumours. Quantitative data will also provide tools for future applications of PEM technology, such as follow-up of patients after cancer therapy.

RESUME

La mammographie par rayons X ne permet pas toujours de différencier les tumeurs malignes et bénignes. Les biopsies pratiquées sur des lésions bénignes sont des procédures coûteuses, et alarmantes pour la patiente. La Mammographie par Emission de Positrons (MEP) repose sur l'injection intraveineuse d'un analogue radioactif du glucose. Les tumeurs cancéreuses, qui ont un métabolisme accru, formeront des points brillants sur l'image MEP.

L'analyse quantitative des images consiste à calculer la quantité de radioactivité absorbée dans chaque sein de la patiente. Après une analyse statistique ROC sur 15 patientes, il a été établi qu'une différence de plus de 10% entre les deux seins peut être interprétée comme un signe de cancer. Grâce à l'application de cette méthode, la précision de l'appareil passerait de 64% à 86%. Cette technique est particulièrement utile dans le cas de tumeurs larges ou diffuses. Elle fournit également des informations nécessaires pour de futures applications de la MEP, comme le suivi des patientes après traitement.

ACKNOWLEDGMENTS

First of all, I would like to acknowledge the much appreciated help of my friend and lab colleague Kavita Murthy, from the very beginning of this project to the final writing phase.

I also sincerely thank my supervisor, Dr C.J. Thompson, who has always encouraged and guided me in my research.

The help of Dean Jolly, from the Cyclotron Unit of the Montreal Neurological Institute has been essential for all the PEM experiments using radioisotopes.

Many thanks go to the X-ray technicians of the Cedar Breast Clinic for sacrificing their lunch breaks so many times to help us during clinical experiments.

The insight of Dr. M. Auger, from the Pathology department, helped me a lot when I was trying to understand the biological characteristics of different tumours.

Merci à Patrick Sciascia, pour son aide et sa bonne humeur pendant les jours de déprime, et pour toute la musique.

Pour leur affection et leurs encouragements au long des deux dernières années, merci à Camille, Anne, Zirke, Suzanne, Simon, et toute ma famille.

Merci à Jean-François. Pour tout.

This work was supported by grant #9232 from the Canadian Breast Cancer Research Initiative of the National Cancer Institute of Canada.

TABLE OF CONTENTS

CHAPTER 1. Biology of breast cancer	4
1.1 <u>Epidemiology and etiology</u>	4
1.2 <u>Basic anatomy of the breast</u>	5
1.3 <u>Benign tumours</u>	6
1.4 <u>Malignant tumours</u>	7
carcinoma in situ	7
invasive carcinoma	7
1.5 <u>Cancer grading</u>	8
1.6 <u>Cancer staging</u>	9
1.7 <u>Glucose metabolism of tumours</u>	10
CHAPTER 2. Current breast imaging modalities	12
2.1 <u>Density imaging</u>	12
X-ray mammography	12
Ultrasound	13
Digital mammography	13
2.2 <u>Magnetic Resonance Imaging</u>	14
2.3 <u>Metabolic imaging</u>	14
Scintigraphy	14
Positron Emission Tomography	15
2.4 <u>Positron Emission Mammography</u>	16
CHAPTER 3. Principles of Positron Emission Tomography	18
3.1 <u>History of PET</u>	18
3.2 <u>PET physics</u>	19
Positron emitting nuclei	19
Annihilation	21
Photon interactions with matter	21
3.3 <u>PET instrumentation</u>	23
Scintillation crystals	23
Electronics and image formation	26
Spatial resolution	27
Energy resolution	28
Timing resolution	28
3.4 <u>PET in oncology</u>	29
FDG in tumours	29

Study of other radiopharmaceuticals	30
CHAPTER 4. Application to Positron Emission Mammography	31
4.1 <u>Development</u>	31
4.2 <u>Physical description</u>	32
General view	32
Crystals	32
PMTs	33
Signal processing	34
4.3 <u>Principles of image reconstruction</u>	35
4.4 <u>Image acquisition and description of PEM software</u>	36
before acquisition	37
acquisition	37
image reconstruction	38
4.5 <u>Co-registration of PEM images and x-ray mammograms</u>	38
CHAPTER 5. Clinical Study	40
5.1 <u>Protocol</u>	40
5.2 <u>Procedure</u>	41
5.3 <u>Decision making for diagnosis</u>	41
5.4 <u>Preliminary results</u>	42
CHAPTER 6. Quantitative analysis of the data	46
6.1 <u>Compartmental model</u>	46
6.2 <u>Standardized Uptake Value</u>	47
6.3 <u>Retroactive correction</u>	49
breast parameters	49
compression	50
patient parameters	50
physical parameters	50
6.4 <u>Asymmetry calculations</u>	52
6.5 <u>Statistical analysis</u>	53
6.6 <u>Results</u>	54
6.7 <u>Programming</u>	56

CHAPTER 7. Parameters affecting PEM images	57
7.1 <u>Contrast resolution</u>	57
7.2 <u>Dead time</u>	59
7.3 <u>Radiation from the heart</u>	61
7.4 <u>Time interval between scans/ first scan and injection</u>	62
CHAPTER 8. Discussion	65
8.1 <u>Diagnostic improvement</u>	65
8.2 <u>Standard procedure</u>	66
8.3 <u>Correlation of asymmetry with tumour parameters</u>	67
8.4 <u>Potential of quantitative analysis for follow-up</u>	69
CONCLUSION	70
References	71

CHAPTER 1.

Biology of breast cancer

1.1 Epidemiology and etiology

After cancers of the skin, breast cancer is the most common cancer among women in the United States and in Canada and the second cause of cancer death (after lung cancer) [1]. In 1998, 19,300 new cases were expected to be diagnosed in Canadian women, of there 5,300 (27%) would lead to death [2]. According to the National Cancer Institute of Canada, age-standardized incidence rates of breast cancer have increased by 20% since 1986 [2]. Over the same period of time, age-standardized mortality rates have decreased by approximately 4%, mainly due to the introduction of routine mammography screenings [2]. In Quebec, it is now recommended that all women of age 50 or more have a mammogram every two years along with physical examination of the breasts by a professional [3].

The causes of breast cancer have not been determined exactly. Several hypotheses are under investigation, such as low-dose radiation exposure, genetic factors [4] or ingestion of dietary fat. Other factors have been proven to increase the risk of developing breast cancer. Among them, the most significant are:

- family history (primary relative with breast cancer)
- menstrual history (early menarche, late menopause)
- being nulliparous, or having first child after the age of 35
- other cancers (e.g., uterus cancer)
- benign breast disease or previous breast cancer
- age (being post-menopausal)

Ethnic factors also seem to play a role, though it is likely to be related to cultural and environmental factors. For example, oriental women have a much lower risk than women in western countries, but women of Japanese descent who reside in the United States have a higher risk than women in Japan [5].

Survival rate is directly related to early detection [5]. The development of screening mammography programs since the mid 1980s has resulted in a significant decrease of the mortality rates. In spite of these efforts, cancerous breast tumours are often more than 2 cm in diameter at time of diagnosis [5]. Novel imaging techniques with high resolution are eagerly investigated in order to serve as a secondary screening tool to complement traditional x-ray mammography.

1.2 Basic anatomy of the breast

The mammary gland consists of 15-20 lobes surrounded by adipose tissue. Each lobe is divided into lobules, which are grape-like clusters of alveoli (milk producing structures). During lactation, milk goes from the alveoli to secondary tubules and then to lactiferous ducts which carry it to the surface of the breast (see figure 1.1 [6]). In clinical practice, four regions of the breast (named quadrants) are defined and 50% of cancers are found in the “upper outer quadrant” [7]. Tumours generally arise from or involve ducts (ductal type) and lobes (lobular type).

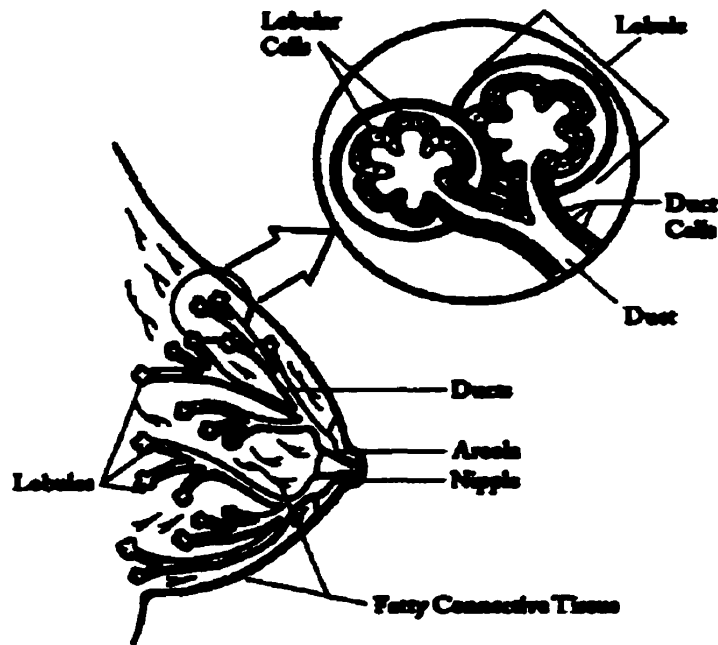


Figure 1.1 : breast anatomy

1.3 Benign tumours

Clinically, a tumour is defined as an abnormal swelling or mass. Cancer is referred to as a “malignant” tumour, while other masses are “benign” tumours. A tumour which is characterized as “benign” is not likely to disseminate outside of the breast and is usually not life-threatening. It can be caused, for example, by an inflammation of tissues.

On mammograms, benign tumours are often mistaken for cancer. In decreasing probability of incidence [8], the most common types are:

- fibroadenoma, which is generally found in young women (20-35 years old).
- intraductal papilloma, found in middle-aged and older women. This tumour grows to a few mm in diameter.
- adenoma of the nipple, which is relatively rare.

1.4 Malignant tumours

a) carcinoma in situ

A malignant tumour is called in-situ when it has not spread beyond its site of origin (for example, for a ductal carcinoma, the tumour has not broken through the duct wall). The most common types are:

ductal carcinoma in situ, which has several variants (comedocarcinoma, cribriform . . . etc.). As its name indicates, it has its origin in the ducts and constitutes 10% of newly diagnosed carcinomas. If cancer is detected and treated at this stage, 98% of patients can lead a disease-free life [5].

lobular carcinoma in situ, which is sometimes considered as a benign disease, since it does not spread in that form, but strongly increases the risk of developing an invasive carcinoma.



Figure 1.2: carcinoma in situ

b) invasive carcinoma

An invasive cancer has already invaded the fatty tissue of the breast and is likely to have caused metastases.

invasive ductal carcinoma is by far, the most common diagnosis (75% of

carcinomas).

invasive lobular carcinoma accounts for 5-10% of breast tumours. The risk of bilaterality (cancer in both breasts) is higher than for ductal carcinomas.

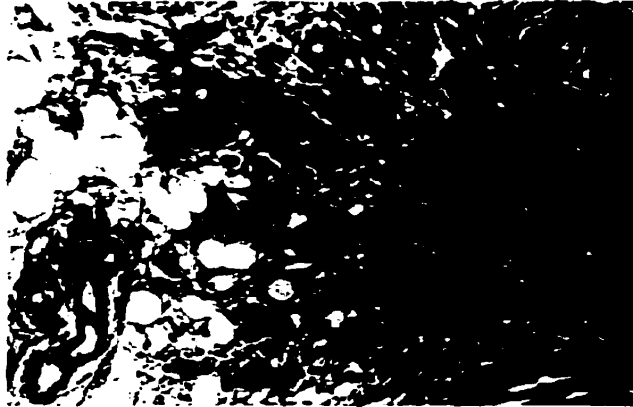


Figure 1.3: invasive carcinoma

Figures 1.2 and 1.3 are reproduced from [7].

1.5 Cancer grading

Histological grading is a way of describing the degree of malignancy of a primary tumour. The grading of a malignant tumour is based upon the modified Bloom-Richardson method [9][10]. After a tissue sample has been collected, three parameters are studied by the cytologist:

Tubule formation: a tubule is said to be well differentiated if a central lumen is visible. A score of 1 is given if more than 75% of the tubules are well differentiated, 2 if 10-75%, and 3 if less than 10% are well differentiated.

Nuclear structure: a score of 1 is given if tumour nuclei are similar in appearance to the normal breast epithelial cells, a score of 2 if tumour nuclei are larger than normal, and 3 if the nuclei are speckled with prominent unusually shaped nucleoli.

Mitotic score: a score from 1 to 3 is given according to the relative number of cell divisions

occurring within a defined tumour volume (1 for a low number, 3 for a high number of divisions).

The overall grade is then obtained by adding up the previous scores.

A grade 1 tumour (well differentiated) corresponds to a total between 3 and 5.

A grade 2 tumour (moderately differentiated) is indicated by a total of 6 or 7.

A grade 3 tumour (poorly differentiated) corresponds to a total of 8 or 9.

The correlation between survival and grade at the time of diagnosis is not well understood at present. Intuitively, the higher the grade, the poorer the prognosis but this hypothesis has not been rigorously confirmed yet [11]. Tumour size is not directly proportional to the grade since some grade 1 tumours can be very large. However, there exists a strong correlation between survival and tumour size.

1.6 Cancer staging

Another important step in the characterization of a cancer is staging: a localized tumour might spread and cause secondary tumours (metastases) to develop in remote areas of the body.

The “TNM” staging system [12] uses three variables :

- the diameter of primary tumour
- the number of lymph nodes involved
- the presence of distant metastases

Survival is directly related to stage at time of diagnosis. The 5-year survival rates are [5]:

97% when cancer is diagnosed at a local stage (in-situ)

76% when cancer is diagnosed at a regional stage (lymph nodes are involved)

21% when cancer has metastasized (in the axial skeleton, the liver, the lung or the pleura)

In the case of breast cancer, the presence of axillary lymph node metastases is the most important prognostic factor [13][14]. Once a breast tumour malignancy is confirmed by cytology, it is essential to know how many lymph nodes (if any) the cancer might have spread to, in order to choose the appropriate therapy. At present, patients almost systematically undergo surgery and removal of the lymph nodes, though they may be healthy. Morbidity associated with this operation includes impairment of shoulder motion, arm swelling or stiffness, and lymphedema [15].

Therefore, there is a need for more than just a primary screening tool. It would be extremely valuable to benefit from a non-invasive imaging modality which would be able to characterize the status of axillary lymph nodes.

1.7 Glucose metabolism of tumours

Glucose metabolism of cancerous cell forms a central part of this study. Glucose from the blood enters the cell by “facilitated diffusion” (i.e., down its concentration gradient with the help of specific proteins, such as Glut-1 transporters). In the cytosol (intra-cellular liquid), the glucose is phosphorylated by the enzyme hexokinase: a phosphor group is added to the glucose molecule in order to form glucose-6-phosphate. The process of phosphorylation increases the energy level of the glucose molecule and also prevents it from exiting the cell.

Under anaerobic conditions, glucose-6-phosphate is degraded through glycolysis, whereby two molecules of ATP (adenosine triphosphate) are produced for each molecule of glucose. ATP is used by the cell as a source of energy.

Under aerobic conditions, the glucose is more efficiently degraded since glycolysis is followed by the Krebs cycle and the electron transport chain, resulting in the production of 32 molecules of ATP per molecule of glucose.

In a tumour, a significant fraction of the cells are hypoxic: their access to oxygen is impaired

due to poor vascularization of tumour tissue. Hence, glucose degradation occurs mainly through glycolysis (anaerobic model). In order to satisfy the energy demand of tumour cells, more glucose molecules are required. This may be why a tumour cell will consume more glucose than a cell in normal aerobic conditions. Several other reasons have been proposed for the increased glucose metabolism of tumours: increased concentrations of hexokinase, decreased de-phosphorylation, increased glucose transporters [16]. . . Though these hypotheses are yet to be confirmed, it is widely recognized that increased glucose demand leads to an increase in glucose uptake of tumour cells compared with normal cells [17].

Metabolic studies rely on the injection of a radioactively-labelled glucose analog. 2-deoxy-glucose is a glucose molecule in which a hydroxyl group is missing on the second carbon. In order to turn the molecule into a radioactive tracer, this missing atom can be replaced by a radioactive isotope of fluorine (^{18}F) or one of the carbon atoms can be replaced by ^{14}C . Labelled deoxyglucose, can undergo the first steps of glucose degradation, i.e. facilitated diffusion and phosphorylation by hexokinase (see figure 1.4). However, deoxyglucose-6-phosphate is not a substrate for further metabolic reactions in the cytoplasm[18]. Moreover, the rate of the de-phosphorylation reaction, which would enable deoxyglucose to exit from the cell, is very low. Therefore, deoxyglucose-6-phosphate accumulates in the cell until its concentration reaches a plateau. The radiation emitted by the tracer can then be used to localize areas of high glucose consumption.

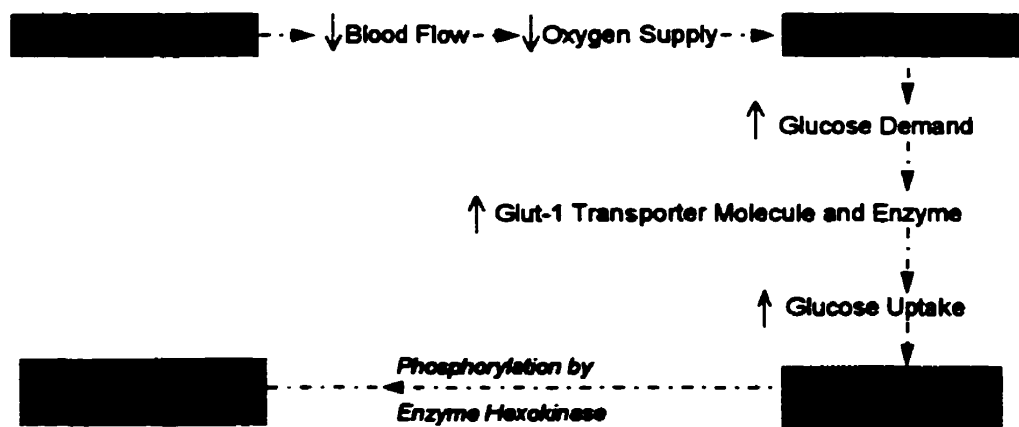


Figure 1.4: increased absorption of deoxyglucose in cancerous cells

CHAPTER 2.

Current breast imaging modalities

Imaging modalities are often compared in terms of sensitivity (i.e., ability to detect cancer in patients who actually have cancer) and specificity (i.e., ability to detect that there is no cancer in healthy patients). The most popular or most promising techniques for detection of breast carcinoma are here briefly described.

2.1 Density imaging

a) X-ray mammography

Principles: this approach relies on the fact that the attenuation rate of x-rays travelling through tissue depends the composition of the tissue. These differences in attenuation within the breast give rise to image contrast: areas of higher density will appear as lucent spots on the x-ray film because more photons are attenuated compared with surrounding lower density tissues. In order to optimize image contrast, low photon energies are desirable though this increases the dose given to the patient. Compression of the breast also considerably improves contrast.

Potential for breast imaging: x-ray mammography is at present the most popular imaging modality for breast cancer detection. Breast tumour cells can produce small amounts of calcium, named “microcalcifications,” which appear as lucent spots on a mammogram. Therefore, radiologists look for clusters of microcalcifications as an indicator for cancer. The spatial resolution of mammography is excellent, allowing the detection of calcifications as small as 0.13 mm [19]. However, in 5-15% of cancers, microcalcifications are absent [20]. Moreover, 65-85% of mammographically suspicious masses turn out to be benign upon biopsy [21]. Indeed, since only anatomical information (density) is available, mammography cannot efficiently distinguish between benign and malignant tumours. These “false alarms” cause unnecessary costs and stress to the patient.

This is of particular concern in premenopausal women, where the presence of thick parenchymal breast tissue reduces contrast resolution by up to a factor of 10 [22]. Approximately 1 out of 4 women will thus be classified as having “radiographically dense breasts” [23]. Therefore, breast cancer detection would greatly benefit from the addition of another imaging modality, that would help bypassing the pitfalls of mammography.

b) Ultrasound

Principles: ultrasonic waves (0.8-15 MHz sound frequency) undergo reflection and refraction when they strike an interface between two different media. Short electric pulses are transformed into mechanical vibrations by a transducer, pressed against the patient’s skin. Echoes (reflections) are produced at a sharp boundary between tissues with different physical characteristics (such as density and compressibility). Reflected vibrations return to the transducer where they are transformed back into electrical signals before being processed to lead to an image.

Potential for breast imaging: Ultrasonography is increasingly used by radiologists as a secondary screening technique for women with dense breasts. A benign fluid-filled cyst and a solid malignant tumour gives rise to rather different echoes upon ultrasonography. In theory, lesions as small as 2 mm can be detected [24], but in practice, this limit is only valid for cysts which provide high contrast relative to adjacent breast tissue. The detection of solid masses smaller than 1 cm is considered unreliable because of the low image contrast they provide [24]. The widespread use of ultrasonography is therefore controversial, since although it is a very simple technique, several studies have reported low sensitivity and specificity [25][26].

c) Digital mammography

Principles: digital mammography provides a flexible, computerized tool for breast imaging. Two approaches are currently investigated. The first consists in digitizing x-rays films acquired in a traditional fashion so that the image may be displayed on a computer screen. This allows the use of several image processing tools to enhance contrast resolution, and of computer-assisted diagnosis

programs. This approach would also be logistically valuable, since film storage would disappear and images could be sent to remote centres if necessary. The second idea is the development of new image sensors, usually involving phosphor detectors, photodiode arrays and fibre optics coupling.

Potential for breast imaging: at present, the potential increase of sensitivity and specificity compared with traditional mammography has not justified the high cost of digital mammography units [27]. More clinical trials are required to assess the potential of this modality.

2.2 Magnetic Resonance Imaging (MRI)

Principles: MRI involves only nonradioactive stable nuclei, mainly protons (from hydrogen atoms in water molecules). These protons are briefly excited by a specific radiofrequency pulse. When this stimulus ends, they tend to go back to their equilibrium condition through a process named relaxation. While relaxing, protons re-emit some radiofrequency radiation that can be processed to form an image according to proton density. One interesting feature is that the relaxation times of water protons depend on the way in which water interacts with surrounding molecules. Thus, some physiological information can be obtained.

Potentials for breast imaging: MRI has been successfully applied to the detection of breast cancer. This approach relies on the injection of a contrast material (such as gadolinium-diethylenetriamine penta-acetic acid or Gd-DTPA) into patient blood, thus providing kinetic (blood flow) and architectural information with high resolution [28]. Although very sensitive (>90%) [28] and supposedly harmless (no ionizing radiation), MRI suffers from relatively low specificity (about 50-60% [29][30]) and high cost.

2.3 Metabolic imaging

a) Scintigraphy

Principles : in an attempt to obtain physiological information on tumour status, research

turned towards nuclear medicine devices. This approach consists in injecting the patient with a radioactively-labelled compound, which mimics a natural molecule preferentially absorbed by cancerous cells. Radioactive atoms in the tracer decay emitting photons, which are collected by a detector. Using back-projection techniques, a map of the radioactivity distribution in the body region of interest is obtained. Single-photon imaging instruments dedicated to breast imaging called scintimammography units are now commercially available. They mainly rely on the use of technetium 99 (^{99m}Tc) Sesta Methoxyisobutal Isonitrile (Sesta-MIBI) as a radiopharmaceutical.

Potentials for breast imaging: the advantages of this technique are: i) Single-photon imaging instruments are already available in the clinics, since their use (e.g., for cardiac imaging) is widespread and ii) ^{99m}Tc is a very convenient radioisotope and is easily produced in a generator from molybdenum. However, the ability of scintimammography to detect lesions smaller than 1 cm has been contested (because of poor spatial resolution), and studies demonstrated a wide range of sensitivities (26-96%) and specificities (about 70%) [31]. Moreover, it is yet to be understood how and to what extent Sesta-MIBI is tumour specific. Finally, the dose to the patient is of the order of 3 mSv (for 30mCi or 1.1 GBq injected) i.e., 4 times higher than for a regular x-ray examination [32].

b) Positron Emission Tomography (PET)

Principles: Positron Emission Tomography uses the same approach as scintigraphy except that it involves “coincidence events”, produced by the simultaneous detection of two 511-keV photons. The physical and physiological principles will be discussed in the next chapter. Briefly, the radioactive atom in the tracer decays by emitting a positron which then annihilates with an electron in the vicinity, thus producing two “annihilation photons”. Unlike some of the previous techniques which can be used to image specifically one region of the body (scintigraphy, mammography, ultrasound), commercially available PET scanners image either the whole body or the brain alone.

Potentials for breast imaging: so far, clinical trials have shown good specificity ([33]:84-97%) and sensitivity (68-94%). However, doing a whole-body PET scan for breast cancer detection is not a cost-effective procedure due to the cost of the scanner itself, the large amount of radiopharmaceutical required (of the order of 350 MBq) and the scanning times (about 1 hour).

Therefore, in spite of its very interesting ability to detect cancer, the clinical use of PET as a routine tool for breast screening is not likely.

2.4 Positron Emission Mammography (PEM)

The cost of PET prevents large-scale clinical application as a secondary screening tool for breast cancer. Some physicians are also concerned about the dose given to the patient. There came the idea of developing of a PET device that would be dedicated to breast imaging. This approach would require a small instrument, reducing the number of detectors involved (hence the cost), and improving the collection efficiency (i.e., decreasing the amount of activity required by a factor of 5).

Feasibility studies [34] demonstrated that such an instrument could have high efficiency and high spatial resolution. Another interesting feature of a breast-specific instrument would be its ability to image the lymph nodes, thus providing a non-invasive tool for staging. Several PEM instruments are being developed worldwide [35][36][37][38]. The first clinical PEM study was reported by Weinberg et al. in 1996 [39].

Table 2.1 : summary of the diagnostic abilities of different breast imaging modalities [40][41].

MODALITY	STRENGTHS	WEAKNESSES	RADIATION DOSE (mSv)	
			Breast	Body
X-Ray mammography *	High resolution High sensitivity	Low specificity	2.7	0.7
Digital mammography*	Computer aided diagnosis	Expensive	2.7	0.7
Ultrasound	Very simple	Low sensitivity and specificity	none	
Scintigraphy	Already available Generator-produced radioisotopes	Low sensitivity for small tumours	-	3
PET (whole body)	High sensitivity and specificity	Expensive	3.7	9
MRI	High contrast resolution	Low specificity	none	
PEM	Expected to have high resolution and high specificity		0.7	0.9

* : regular 2-view bilateral screening

CHAPTER 3.

Principles of Positron Emission Tomography

3.1 History of PET

The earliest use of radionuclide imaging dates back to the early 1960s. Single-photon tomography was developed by Anger in 1961 [42] and demonstrated its potential for quantitative physiological studies.

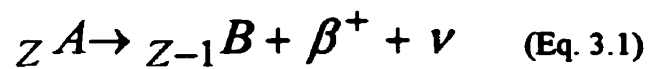
Approximately 30 years ago, it was proven possible to localize a positron-emitting radionuclide by detecting the resulting annihilation photons [43]. Image reconstruction algorithms started being developed for this purpose. This technique was called “Positron Emission Tomography” or PET. In the most common design for PET, detectors form a ring around the patient, who was either injected with or asked to inhale an agent containing radioisotopes. PET has been used extensively in functional studies of the brain (blood flow, blood volume . . .) or to provide non-invasive information about diseases such as Parkinson, Alzheimer or cardiac disorders. Because of its ability to image tumour metabolism, PET also provides new tools for cancer detection, staging and monitoring.

Last year, the use of fluorodeoxyglucose (see section 3.4) for tumour imaging with “whole body PET” was approved for reimbursement by medical insurance agencies in the USA. This is expected to have a significant influence on the development of PET for diagnosis and staging of cancer.

3.2 PET physics

a) Positron emitting nuclei

Some nuclei are unstable because they have an excess number of protons compared to their number of neutrons. They stabilize by ejecting a particle called a positron (same mass but opposite charge of an electron). This process is referred to as “ β^+ decay”. The kinetic energy produced in this reaction is split between the positron and a simultaneously ejected neutrino.



where A is the parent nucleus, B is the progeny nucleus and Z is the atomic number.

Positron emitting nuclei are produced in particle accelerators, such as cyclotrons, where a neutron is removed from the parent nucleus. The most common positron-decaying isotopes used in PET are listed in table 3.1.

Table 3.1: some positron-decaying isotopes and their characteristics [44][45]

Radio-isotopes	Half-life in min	Maximum positron energy (MeV)	Positron radial range in water (FWHM)	Labelled Compound	Application for imaging
^{18}F	109	0.64	1.02 mm	fluoro-deoxyglucose	glucose metabolism
				fluoro-dopa	ligand-receptor studies
^{11}C	20.3	0.96	1.11 mm	^{11}CO	cerebral blood volume
				$^{11}\text{CH}_3\text{I}$	receptor studies, protein synthesis
^{13}N	10	1.19	1.42 mm	$^{13}\text{NH}_3$	organ perfusion, metabolism
				13N-amino acids	amino acid metabolism
^{15}O	2.1	1.72	1.7 mm	H_2^{15}O , C^{15}O	cerebral blood flow
				C^{15}O_2	cerebral blood volume
				$^{15}\text{O}_2$	oxygen consumption

b) Annihilation

The positron loses its kinetic energy in interactions with atoms in the medium, and then annihilates with one free electron to produce two anti-parallel photons, each with 511 keV energy (this energy comes from the mass energy of the positron-electron pair). Because of momentum conservation, these photons are not travelling in exactly opposite directions (180 degrees \pm 0.25°) [46] and this approximation has repercussions on spatial resolution, as will be discussed in section 3.3.c.

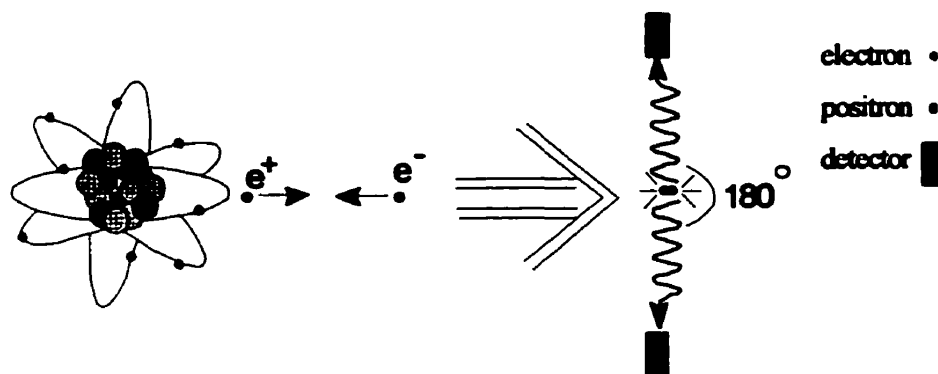


Figure 3.1: positron-electron annihilation

Figure 3.2 is taken from [47]

c) Photon interactions with matter

Compton scattering

Photons may interact with electrons or atoms in tissue before they reach the detectors. At 511 keV, in tissue, the main interaction process is called Compton scattering. It involves a photon and a

free or loosely bound electron. Some energy is transferred to the electron and the photon is scattered at an angle θ .

The general equation for Compton scattering [48] is:

$$h\nu' = \frac{h\nu}{1 + \frac{h\nu}{m_0c^2} \times (1 - \cos\theta)} \quad (\text{Eq. 3.2})$$

where $h\nu$ is the energy of the incident photon, $h\nu'$ is the energy of the scattered photon and m_0c^2 is the mass energy of the electron (511 keV). θ can vary between 0 and 180°. Scatter influence on the image will be discussed in section 3.3.d.

Photoelectric effect

Although this interaction process has a relatively small probability of occurrence in tissue for 511 keV photons, it becomes important when photons reach the detectors, and will be discussed briefly. The photoelectric effect is a photon-atom interaction. One bound electron of the atom totally absorbs the energy of the incoming photon. This so-called photoelectron will then be ejected out of its original atom shell with a kinetic energy equal to $h\nu - E_B$, where $h\nu$ is the energy of the incoming photon and E_B is the binding energy of the electron shell. The vacancy created in the electron shell leads to the emission of characteristic radiation or Auger electrons. The kinetic energy imparted to the photoelectron is deposited in the vicinity by ionization and excitation interactions.

The probability of photoelectric interaction increases in high atomic number materials.

Total attenuation

Overall, if all interaction processes are considered, a photon beam is attenuated in matter in

an exponential fashion. In an absorber of thickness t , the attenuation equation [48] is:

$$N(t) = N_0 \times e^{(-\mu t)} \quad (\text{Eq. 3.3})$$

where $N(t)$ is the number of photons transmitted through a thickness t , N_0 is the number of incident photons and μ is called the linear attenuation coefficient. For 511 keV photons in water-equivalent tissue, the attenuation coefficient is $\mu = 0.097 \text{ cm}^{-1}$ [48].

3.3 PET instrumentation

a) Scintillation crystals

The detection of high-energy photons relies on the use of “scintillators”, which transduce the radiation into visible or ultraviolet light. Generally, these scintillators are crystals such as sodium iodide (NaI), bismuth germanate (BGO) or lutetium oxyorthosilicate (LSO). Photons interact with crystals by Compton scattering and photoelectric effect. The photoelectric effect provides more useful information about the position and total energy of a detected photon since the energy of the incident photon is completely absorbed in one interaction. Therefore, a good scintillating material should offer a high probability for photoelectric interactions versus Compton scattering.

The principle of scintillation is best described by means of the band theory of solids (see figure 3.2). In a pure crystal, the valence band is normally filled with electrons while the conduction band is empty. These bands are separated by a “band gap” or “forbidden band of energies” of the order of a few electron-volts. The electrons excited from direct interaction with 511 keV photons ionize or excite many atoms in the valence band of the scintillator, thus leading a large number of electrons to reach the conduction band. Thus, so-called “electron-hole” pairs are created. In order to be efficient as a scintillator, the crystal should not be pure but should present impurities which will act as activator sites. The decay of an activator state (electron in activator site going back to ground state) produces a photon in the visible or UV region. Thus, the interaction of a single 511 keV results a very large number of decays and produces a scintillation signal that can then be processed.

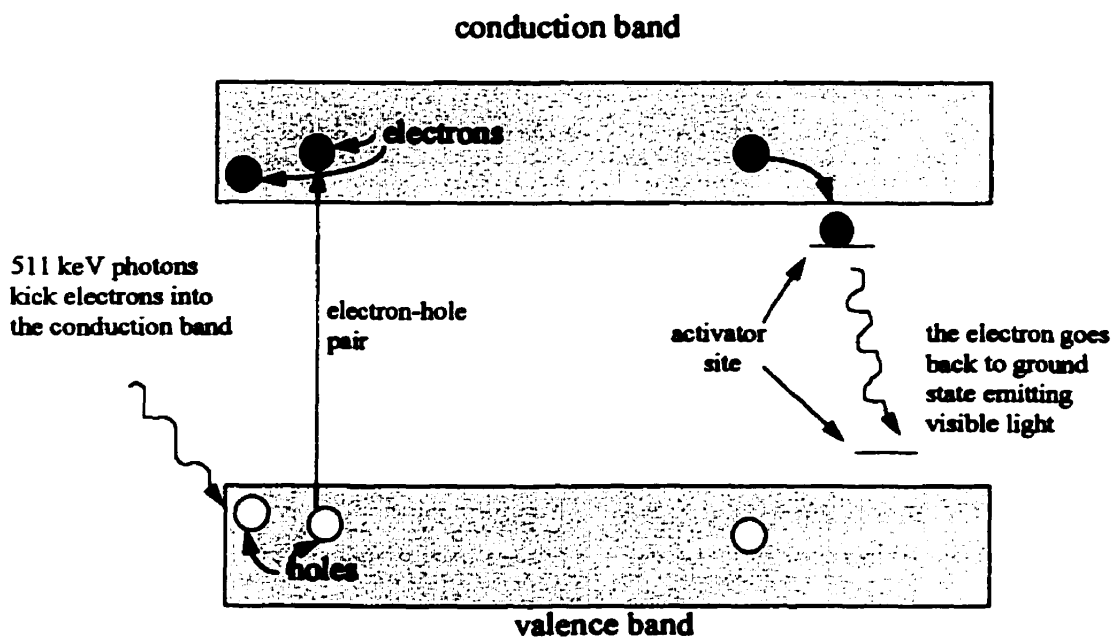


Figure 3.2: principles of scintillation

Several types of scintillation crystals are now available on the market. Their characteristics are described in table 3.2. Ideally, a scintillator should have a high atomic number (to favour the photoelectric effect versus Compton scattering), and should provide a high light output as well as a fast decay time for scintillation light. Some intensive research is being carried out to investigate the potentials of “sandwich detectors”, made of layers of different crystals.

Table 3.2: characteristics of different scintillation crystals [49][50][51]

Properties	LSO	NaI(Tl)	BGO	CsF	GSO	BaF ₂
Z effective	66	50	74	53	59	54
Density (g/cm ³)	7.4	3.67	7.13	4.61	6.71	4.8
Scintillation decay time (ns)	40	230	300	2.5	60	0.8
Total linear attenuation coefficient at 511 keV (cm ⁻¹)	0.87	0.34	0.92	0.44	0.67	0.47
Refractive index at peak emission	1.82	1.85	2.17	4.61	1.9	1.57
Hygroscopic	no	yes	no	yes	no	a little
% light yield relative to NaI(Tl)	75	100	8 - 12	3 - 6	14-20	5 - 16

b) Electronics and image formation

The light signal retrieved from the scintillation crystals is too weak to be processed as such. Photomultiplier tubes (see figure 3.3), or PMTs are required to amplify this signal up to 1 million times. The first-stage level of the PMT comprises a photocathode (usually covered with cesium-antimony or potassium-cesium-antimony) which converts photons into electrons with an efficiency of 10 to 30%. This photocathode focuses the photoelectrons to the input of a dynode chain, usually containing 9 to 12 elements. Each element is at positive voltage with respect to the preceding one in the chain, so that electrons are attracted to the next dynode. The potential difference between the cathode and the last dynode is usually of the order of -1.2 kV. For one electron collected, each dynode will typically produce 2 or 3 secondary electrons, causing a shower of electrons to be collected at the anode. Magnetic shielding of the PMT is required to prevent the electrons from being deviated from their path between the dynodes.

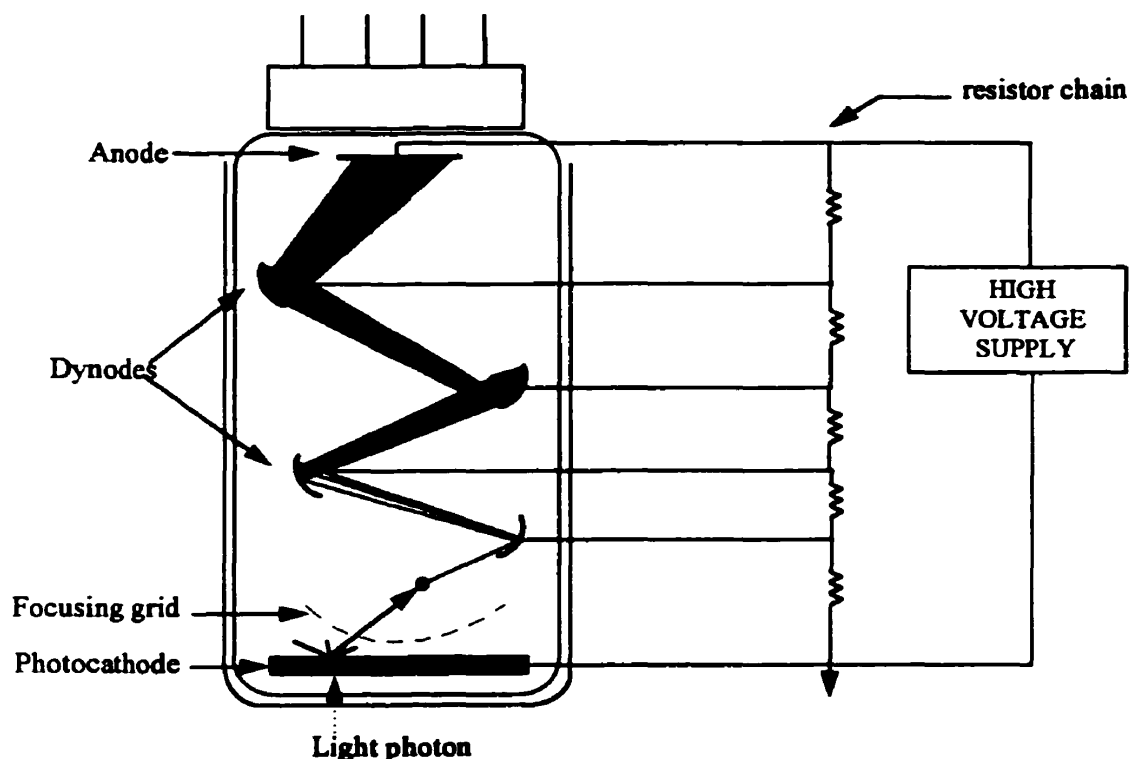


Figure 3.3: photomultiplier tube.

The PMT output then undergoes a series of amplification before the information, that is, the position of the scintillation event and the energy of the incoming photon, is processed. These data allow the reconstruction of the image with “filtered back-projection” techniques. A projection of the imaged object is actually acquired and powerful algorithms (similar to those used in Computerized Tomography (CT) imaging) handle many of these projections to get back to the original distribution.

c) Spatial resolution

Spatial resolution is defined as the smallest separation (Full Width at Half-Maximum or FWHM) at which two signal sources can be placed and still be detected. Several inherent factors limit PET resolution:

- *positron range*: electron-positron annihilation does not occur at the site of positron emission, because the positron travels a short distance (a few mm) in the medium before losing its kinetic energy and meeting an electron (see figure 3.4). This distance depends on the energy of the emitted positron (see table 3.1).

- *anti-parallel photons*: annihilation photons are not exactly 180° apart and the anti-parallel approximation is wrong by +/-0.25° (see figure 3.5). For a typical PET ring of 25 cm in radius, a 0.25° error in the centre results in a blurring of $(250 \text{ mm} \times \tan(0.25^\circ)) = 1.1 \text{ mm}$. This effect increases with detector separation.

- *intrinsic detector resolution*: this factor includes scintillation photon statistics, imprecision of the readout and the dimensions of the crystals. Therefore, it can be controlled to some extent.

The spatial resolution is also affected by Compton scattering of the photon within the detector, light spread in the crystals or at the front face of the PMTs . . . , etc. Commercially available PET scanners have a resolution of the order of 5 mm.

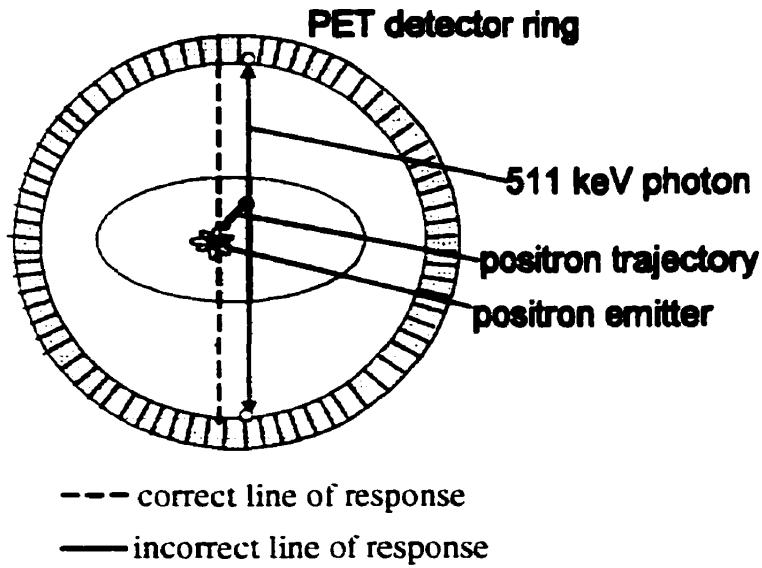


Figure 3.4: effect of positron range on spatial resolution [47].

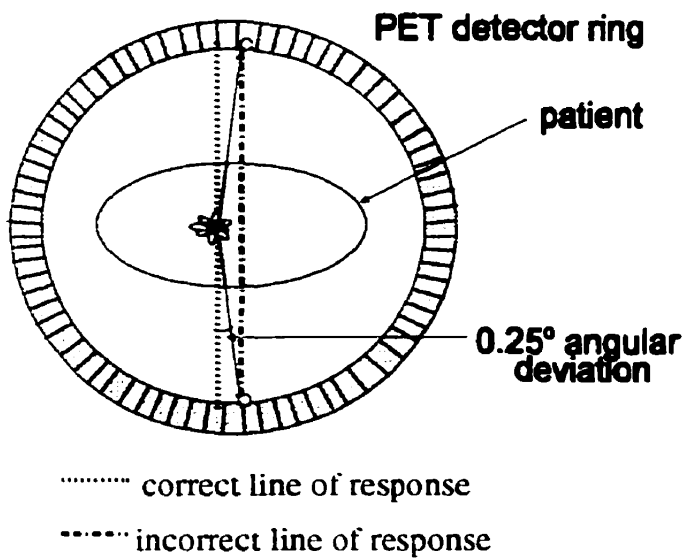


Figure 3.5: loss of resolution due to non collinearity of annihilation photons [47].

d) Energy resolution

The energy resolution of a PET system describes its ability to distinguish 511 keV photons from those with lower (or higher) energies. As discussed in section 3.2.c, annihilation photons can undergo Compton scattering in the medium. The resulting Compton photon has a different direction (and lower energy) than the original 511 keV. This may result in a mis-localization of the annihilation and a blurring of the final image.

Ideally, all scattered photons should be eliminated to obtain a perfect image, and this could be done by rejecting all incoming events with energy lower than 511 keV. However, because of its limited energy resolution, the system might not be able to distinguish between a 511 keV photon and, say, a 503 keV one which would have undergone a 10° Compton scattering (according to equation 3.2). For comparison, a 45° Compton scattering would result in a photon energy of 395 keV. Therefore, photons can scatter through a relatively large range of angles before there is a significant loss in energy. Consequently, scatter can never be completely eliminated.

By determining an “energy window” for acceptable events (with energy close to 511 keV), it is possible to ignore a significant fraction of the lower energy scattered photons or higher energy events which actually result from the pile-up of several events. A narrow energy window (taking into account the energy resolution of the system) would eliminate most scattered photons and improve image quality; however, there is a risk that accepted events are then too few to form a useful image. On the other hand, a wide energy window may lead to degradation of image quality because of scatter. Therefore, a trade off is necessary in order to obtain meaningful diagnostic images.

e) Timing resolution

As previously said, Positron Emission Tomography relies on the simultaneous detection of the two photons produced by one electron-positron annihilation event. Background noise in the image can be produced by “random events”, which occur when two photons from different annihilation events strike detectors at the same time and are recorded as a coincident event (see figure 3.6). These photons may not arrive exactly simultaneously, but neither do true annihilation photons. In order to

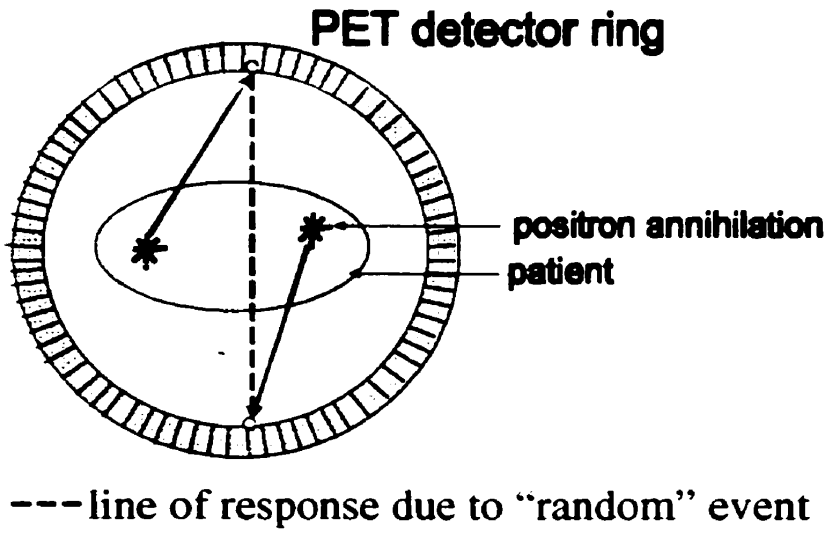


Figure 3.6: example of erroneous “random” event

minimize the number of random events, it is essential to have a good timing resolution: the system should be able to detect the delay between different arrival times and to reject the event if this delay is over a certain threshold value.

3.4 PET in oncology

Radioactive compounds are chosen so that they can mimic real physiological processes. In oncology PET, ^{18}F -Fluoro-deoxyglucose (^{18}F -FDG), which is a glucose analog, is favoured because of its convenient half-life (110 min) and its good tumour affinity [52].

FDG synthesis requires a cyclotron to produce ^{18}F . Protons (or deuterons) are accelerated in order to achieve a wide range of kinetic energies. The proton strikes an oxygen (^{18}O) gas target and the following reaction occurs:



^{18}F is then conducted through a pipeline to a hot cell in the chemical laboratory for FDG synthesis.

a) FDG in tumours

Fluoro-deoxyglucose is a glucose analog. As discussed in section 1.7, FDG is recognized by the enzyme hexokinase and is phosphorylated. However, it cannot go through the succeeding steps of glycolysis and slowly accumulates in the cell.

Because tumours have a higher need for glucose, more FDG is stored in cancerous cells than in healthy tissue. In breast cancer patients, Wahl and al. [53] have shown a tumour-to-background uptake ratio ranging from 1.8 to 800, with an average of 8.1:1. These data clearly show the

interesting properties of FDG as a cancer marker.

Beside malignant tumours, FDG is absorbed by other metabolically active organs in the body. For example, the brain and the heart both show high affinity for FDG, and radiation from these regions can impair image contrast (which is the visible absorption difference between tumours and surrounding healthy tissues). Moreover, FDG uptake, as glucose consumption, depends on other physiological factors, such as tissue oxygenation or regional blood flow.

b) Study of other radiopharmaceuticals

The main drawback of FDG is its tumour nonspecificity. A recent article [54] has demonstrated that other ^{18}F -labelled agents could be more suitable for breast cancer imaging because their tumour-to-background uptake ratio would be higher. ^{11}C -labelled compounds (mimicking, for example, protein synthesis) have also been proposed, but the resulting image contrast is not as impressive as with FDG.

In addition, there exist economical limitations to the widespread clinical use of FDG. The cyclotron is an extremely expensive piece of equipment and only 5 of them are in operation in Canada at present. Imaging modalities relying on the use of cyclotron-produced radioisotopes would then only be available to patients living close to a cyclotron unit. However, the half-life of FDG is quite long (110 min) compared with other radioisotopes, and this feature enables FDG to be delivered from a cyclotron site to some remote clinical centres. It is estimated that more than 70 % of the Canadian population lives within a 2-hour drive of a cyclotron centre and would therefore have access to FDG [55].

Nevertheless, some research is being performed in order to find generator-produced radioisotopes suitable for PET imaging, as it would reduce scanning costs. Studies have been done on gallium 68-somatostatin analogs. ^{68}Ga (half-life=68 min) is a progeny of ^{68}Ge , for which a generator is available. This radiopharmaceutical exhibits affinity for tumour receptors [56]. Therefore, it would be more tumour-specific than FDG and would be less influenced by patient parameters (such as presence of natural glucose in the blood). More research is needed to investigate the potential of ^{68}Ga -labelled tracers for breast carcinoma detection.

CHAPTER 4.

Application to Positron Emission Mammography

The PEM-1 scanner (see figure 4.1) was designed to apply the principles of PET solely to breast imaging. In this instrument, two detectors are placed very close to the breast tissue in order to provide three-dimensional and high-resolution images with a small amount of activity (75 MBq) and short imaging times.

4.1 Development

The idea of a dedicated breast imaging unit using PET principles was originally patented by Weinberg et al. in October 1993 . C.J. Thompson was then consulted to assess the feasibility of a PEM system and demonstrated, using Monte-Carlo simulations, that the instrument would have high efficiency and a spatial resolution about 2 mm [57]. A second patent was obtained for this more detailed system [58].

In 1994, K. Murthy determined the optimal crystal thickness of the detectors. One year later, the final design for crystal configuration was established as an array of bismuth germanate oxide (BGO) crystals, cut in an offset grid pattern (this feature is described in section 4.2.b). C.J. Thompson and Y. Picard showed, again by Monte-Carlo simulations, that scanning times of the order of a few minutes would give good quality diagnostic images.

Several improvements such as enlargement of the field of view, and corrections for spatial distortions and image uniformities were made respectively by R. Clancy and J. Robar between 1994 and 1996 [59][60]. In the meantime, A. Bergman developed a technique to co-register PEM images and x-ray mammograms [61]. The first prototype, called PEM-1, is now into phase I of clinical trials. At present, 15 patients have been scanned, and the strengths and weaknesses of the existing instrument have been clearly determined.

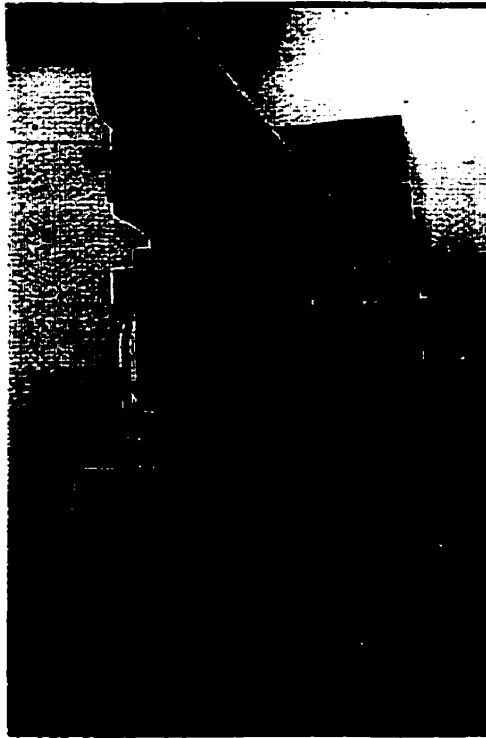


Figure 4.1: picture of the PEM-1 scanner inserted into the mammography unit at the Cedar Breast Clinic, Royal Victoria Hospital.

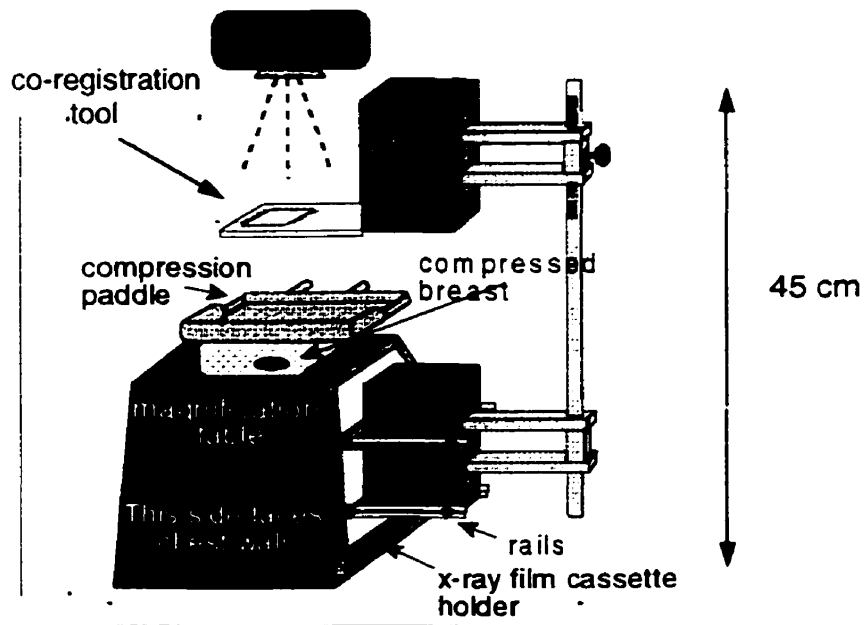


Figure 4.2: PEM-1 features [47].

The work presented here is the quantitative analysis of patient images acquired with PEM and has contributed to

- 1) evaluate the contrast between FDG uptake by tumours and by healthy tissues,
- 2) point out the factors that may have caused some false PEM diagnoses,
- 3) elaborate a standard scanning procedure so that a higher sensitivity can be expected,
- 4) provide tools for future studies, such as follow-up of patients after therapy.

4.2 Physical description

a. General view

The PEM-1 scanner is approximately 45 cm x 30 cm x 20 cm. A schematic drawing is presented in figure 4.2. The base consists of a hollow trapezoidal table shielded with lead. The breast rests on top of this “magnification table”. The mobile element of PEM-1 is made of a pair of detector boxes, containing the scintillation crystals and the PMTs. Both detectors are mounted on a vertical support and this assembly can slide laterally. The lower detector slides in and out the magnification table, and the upper detector moves over the breast. If the instrument is inserted into a mammography unit, this translation allows to acquire x-ray mammograms (when detectors are slid OUT: figure 4.3) and PEM images (when detectors are moved IN: figure 4.4) without repositioning the patient. The upper detector can also move vertically along the support, in order to adapt to different breast compressions.

b. Crystals

The PEM detectors have been designed so that the instrument would fit into the standard “Philips Mammo DIAGNOSTIC-UC” mammography unit in use at the Royal Victoria Hospital. This set-up is shown in figure 4.1. While scanning, the upper detector is placed between the x-ray tube and

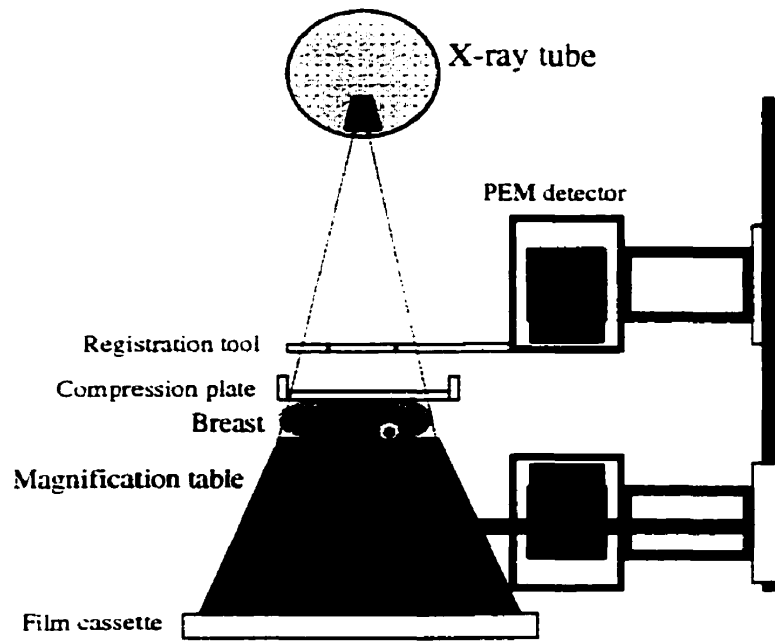


Figure 4.3 : in position for mammography [47]

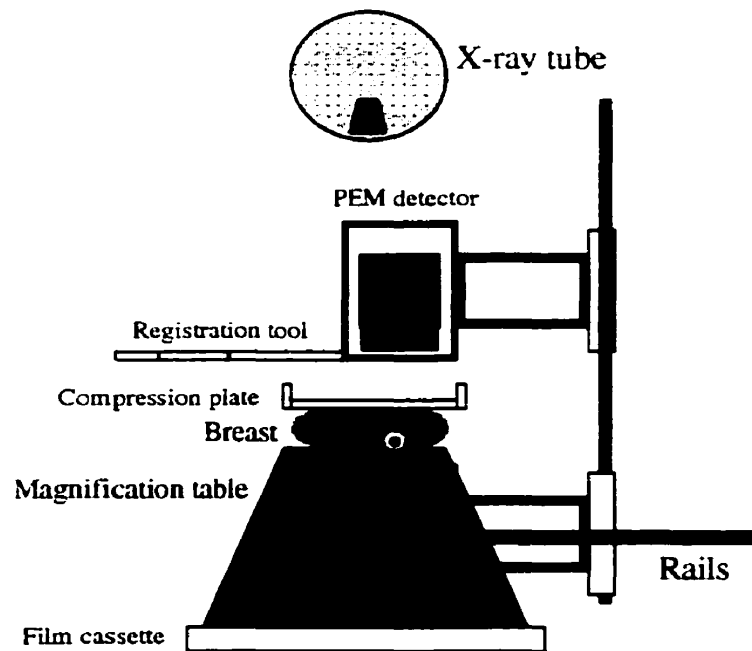


Figure 4.4: position for PEM acquisition [47]

the mammography compression plate whereas the lower detector must fit between the patient's lap and her breast. The magnification table commonly used in mammography has been modified to house the lower PEM detector.

Physically, each detector is made of 4 BGO crystal blocks whose dimensions are 36 x 36 x 20 mm. Crystals have been cut on both surfaces in 2 x 2 mm squares using a multiple blade diamond saw (see figure 4.5). Cuts on the bottom are offset from those on the top by 1.0 mm. In order to keep the same probability of photon interaction in both layers of the crystals, the bottom layer must be thicker than the top layer, which has already attenuated the photon beam. More precisely, this depth is 11.5 mm for the elements facing the PMTs and 6.5 mm for elements facing the imaged subject. There is a 2-mm uncut region between these two layers. The gaps between crystal elements are polished by acid etching and filled with opaque light-reflecting material so that photons are "channelled" to the surface of the photomultiplier tube. This "pixellation" technique allows to get one bit of depth-of-interaction information by identifying the layer in which scintillation events occur and to double the spatial sampling of the block (see figure 4.6). Because of the offset between top and bottom elements, the sampling interval is 1 mm even though the crystals are twice this width.

Each detector is thus made of 2312 crystal elements. The detectors are shielded with 10 mm of lead in order to reduce the amount of extraneous radiation reaching them.

c. PMTs

The scintillation crystals are coupled to the front face of the PMTs by a thin layer of resin (SYLGARD 186, Dow Corning, MI, USA). This glue was chosen for its good properties as an optical coupling between BGO and the PMTs, in order to minimize the light loss at this interface. In addition, this coupling must be strong enough so that crystals and PMTs stick together in spite of gravity when the PEM detectors are positioned at various angles.

PEM photomultiplier tubes are Hamamatsu R3941-05 position sensitive PMTs (PS-PMTs).



Figure 4.5: crystal elements of a PEM detector

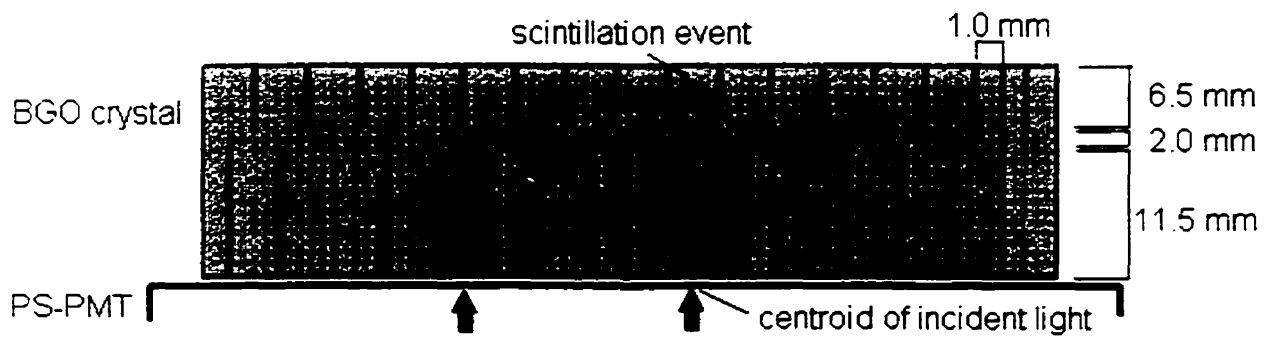


Figure 4.6: offset technique. The difference between a scintillation event occurring in the top layer and one in the bottom layer is shown [47].

They have a front area of $7.5 \times 7.5 \text{ cm}^2$ and a useful field of view of about $6.5 \times 5.5 \text{ cm}^2$. A PS-PMT uses a crossed-wire anode with 18 wires in the X direction and 16 wires in the Y direction, with respective pitches of 3.75 and 3.70 mm. Compared to conventional PMTs described in 3.3.b, a PS-PMT offers the advantage to ensure that there is a correspondence between the centroid of the charge collected by the wires and the location of the scintillation event. This feature provides spatial localization.

All wires are connected in an Anger-type resistor chain readout which produces x^+ , x^- , y^+ , y^- (position of scintillation event) and energy information. The resistor chain is designed to weigh the contribution from each anode wire and has been modified to reduce non-linearity at the edges of the field of view [59].

d. Signal processing

In our case, the X direction is parallel to the patient chest, while the Y direction is perpendicular (the Z direction would be a vertical line going through the patient's breast). The X and Y positioning signals are formed by computing $X = (x^+ - x^-)/E$ and $Y = (y^+ - y^-)/E$ where E is the event energy equal to $(x^+ + x^- + y^+ + y^-)$. Meanwhile, timing signals coming from the last dynode of the PMTs are analysed by constant fraction discriminators and a coincidence circuit, in order to sort out the "true coincident events" These events result from the detection of the two photons originating from one electron-positron annihilation. The coincidence module was designed and fabricated in-house.

True coincidences are used to trigger an Aurora-14 6-channel "Computer Automatic Measurement and Control" (CAMAC) Analog-to Digital Converter (ADC) from Jorway Corp., Westbury, NY, USA. This ADC, which digitizes X, Y and E signals from each detector, is interfaced to an Alpha model 4/100 200 workstation via a Small Computer System Interface (SCSI). There, the computed X, Y and E values are stored sequentially in a list file as 8-bit numbers (see figure 4.7).

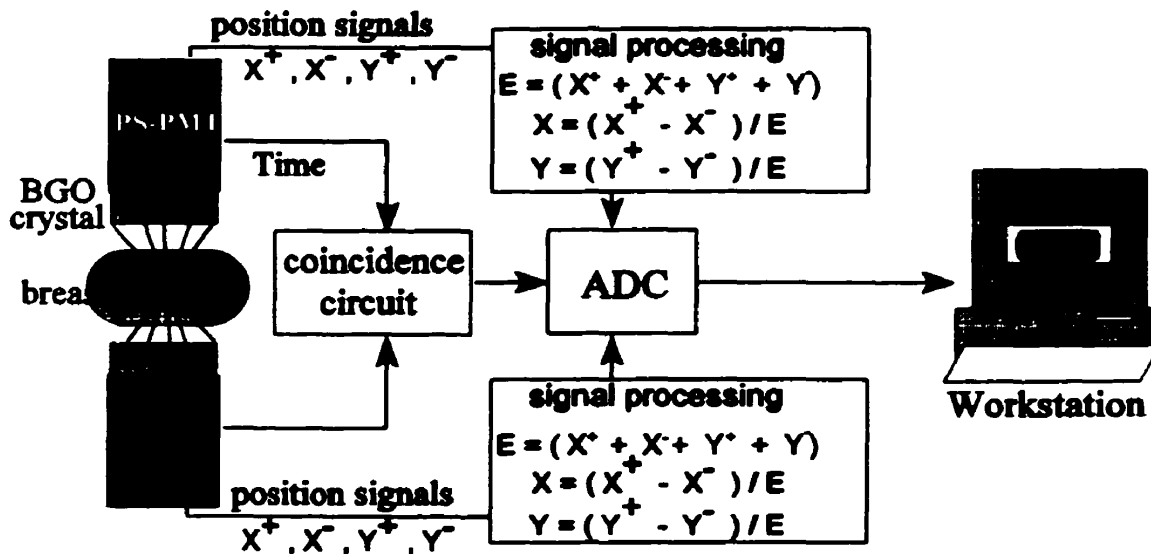


Figure 4.7: hardware for the PEM system [47]

4.3 Principles of image reconstruction

PEM uses a simple “line-of-response” (LOR) technique for image reconstruction as opposed to the filtered back-projection used in conventional PET. A line, called the LOR, is drawn between the two crystals involved in one coincidence detection and the annihilation event is known to have occurred along this line. The breast thickness is virtually divided in seven layers, with one image plane per layer. The LOR intersects with each plane, and the image is then reconstructed as if annihilation events occurred in each one of these seven planes (see figure 4.8). Corrections are applied for:

- photon attenuation along the line of response
- probability that an event occurs in any one particular plane (in order to preserve image uniformity even if the probability of detection is higher for an event occurring at the centre of the FOV)
- crystal efficiencies (inside the same detector block, some crystals are much more efficient in

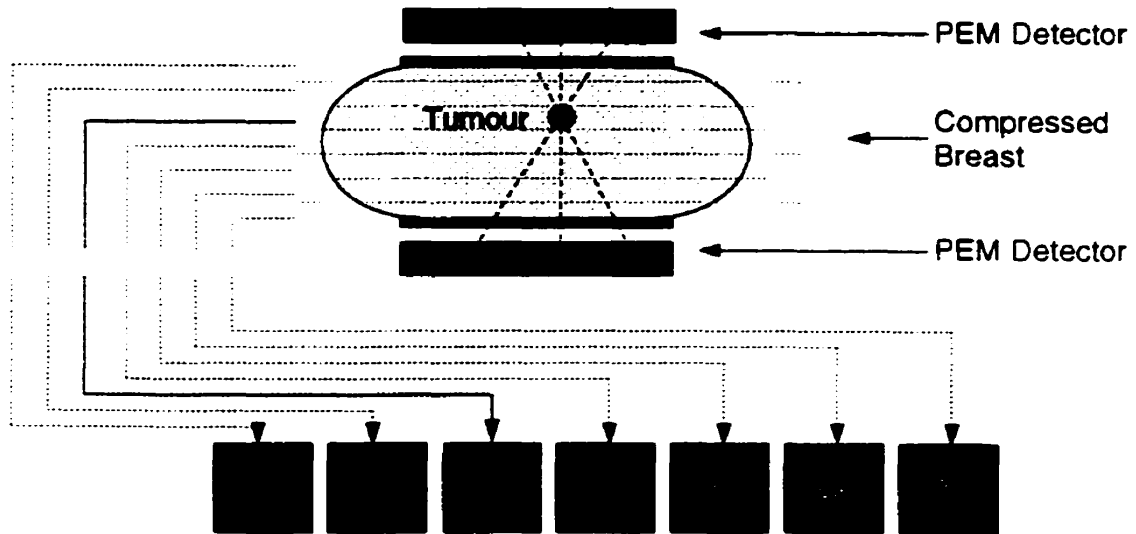


Figure 4.8: the image of the tumour is reconstructed in each plane.

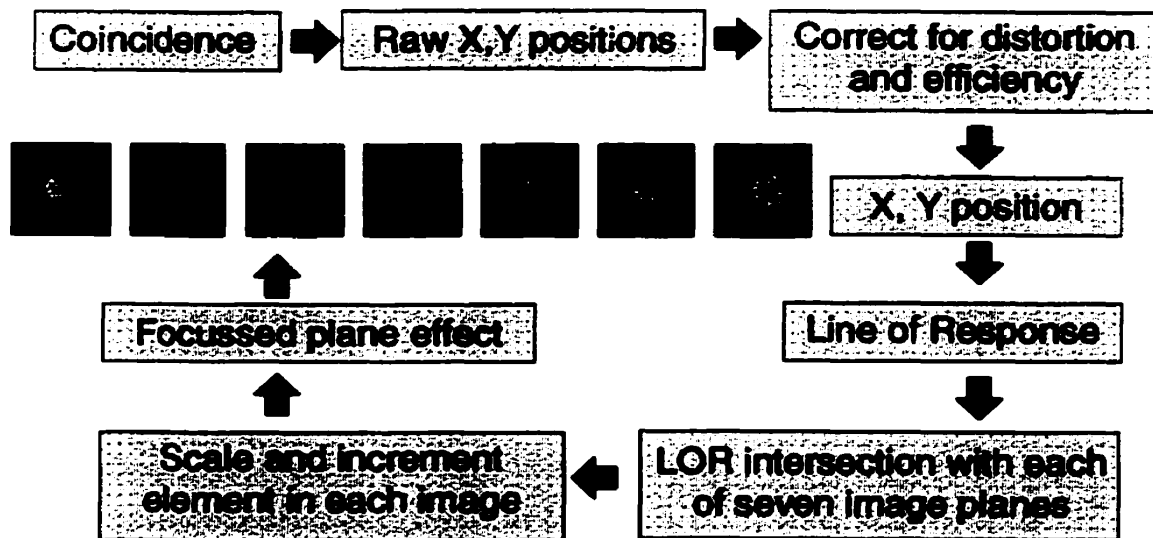


Figure 4.9: reconstruction of the image and focussed plane effect.

terms of detection of a photon than others)

- spatial distortions introduced by the PMTs and their associated electronics (due partly to charge truncation at the edges of the anode)
- gain nonuniformity of the PMTs (which introduces of spatial dependence on the measured energy signal at the output of the PMT)

For the last three phenomena, parameters are stored in independent Look Up Tables (LUT). More details on this work are available in J. Robar's paper [60].

The plane in which the image would be the most focussed is then supposed to give the location of the radioactive source (see figure 4.9). This technique allows to have 3D information while keeping the time required for image reconstruction very short.

4.4 Image acquisition and description of PEM software

The PEM software consists of three interdependent programs (PEM_COM, PEM_ACS, PEM_DIS) written in Fortran 77, and running on an Alpha station under a VMS operating system. The main control program is called PEM_COM and its links to the other programming units are shown on figure 4.10.

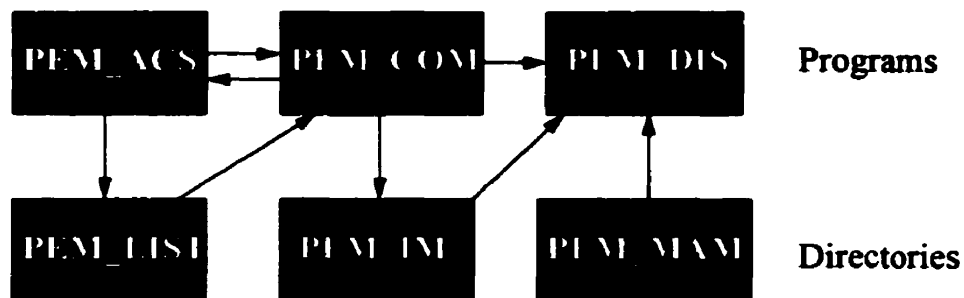


Figure 4.10: links between PEM programs and directories.

a) before acquisition

The user must fill in some parameters such as patient identification, compression used, scan duration and energy window. This last feature is related to the energy resolution described in section 3.3.d. For example, an energy window of 350-650 keV would result in rejecting photons with detected energy lower than 350 keV or higher than 650 keV. On the control window, two numbers of counts are displayed: the “detected counts” are independent of the energy window and represent all the coincidence events perceived by the system, and the “accepted counts” represent those of the detected counts which fall within the energy window in both detectors.

b) acquisition

PEM_ACS receives the X, Y and Energy information. During a scan, images are displayed in real-time by PEM_DIS and the user is free to choose to either create a simultaneous list file (saving the data and thus enabling to display the image again later) or not. The list files, if created, contain 3 bytes of data per detector (one byte for each information X, Y and E). Data are transferred from the ADC buffers to the list file every 1024 events (this procedure takes approximately 4 ms per transfer).

List files are stored in a dedicated directory called PEM_LIST, while images are stored in PEM_IMA.

c) image reconstruction

PEM_DIS opens the window in which the seven planes of the image will be displayed. This window enables the user to choose several imaging processing options such as the colour scale, zoom or profile drawing. Two sets of images can be displayed on the same window in order to compare, for example, both breasts of the same patient. The general program, PEM_COM can handle three different situations:

- *The image is being acquired.* In that case, the user is free to choose to perform a quick acquisition without storing the image, or to save the data. In this last case, a list-file is created in PEM_LIST and the image itself is saved in PEM_IMA. During the scan, the “live” display on the computer screen is updated every 2 seconds.

- *The image from a previous scan is displayed.* PEM_COM can re-display an image that has been saved in PEM_IMA and read data related to the scan (such as duration, number of buffers allocated, energy window . . . etc.).

- *The image from a previous scan is reconstructed from the list-file.* This situation occurs for example when the user wants to visualize a previously acquired image with a different energy window than the one used during the scan.

4.5 Co-registration of PEM images and x-ray mammograms

The co-registration technique has been developed by Alanah Bergman and is briefly described here: the reader is referred to her paper [61] for a more complete discussion on this method. The purpose of co-registration is to make sure that the hot-spot on a PEM image corresponds to the mass identified on the x-ray mammogram. This process relies on the use of a registration tool, consisting

of a plexiglass plate in which a wire defines a rectangle. This tool is attached to the PEM detectors in such a fashion that the rectangle defines, when the PEM detectors are slid “out”, the area that would represent the FOV of PEM if the detectors were slid “in”. Since the patient is not moved between x-ray imaging and PEM acquisition, the images can be superposed (see figure 4.11).

PEM images must be scaled prior to superposition because the cassette of the x-ray film is located below the magnification table, yielding a greatly magnified image of the breast, whereas PEM images are not magnified. A program has been integrated to the PEM software to allow computed co-registration. The x-ray mammogram is digitized by means of a light box and a video frame grabber connected to the Alpha station. The “register” function on the display window enables the user to overlay the PEM image on the mammogram. The procedure consists of four phases: 1) the user selects the appropriate gray-scale on the mammogram image, 2) with the mouse, the user drags and stretches a rectangular outline of the co-registration tool until it overlays the tool’s image on the x-ray image, 3) the registration program finds the corresponding scaling factor to be applied to the PEM image, 4) the program display the colour PEM image on top of the black-and-white x-ray image.



Mammogram



PEM +Mammogram

Figure 4.11: co-registration. The hot spot of the PEM image is overlaid on the mammogram [47].

CHAPTER 5.

Clinical Study

Our group started to scan patients on January 1997. I participated in the last two clinical scans to date. All subjects signed an informed consent form and were free to withdraw from the study at any time. Scans took place at the Cedars Breast Clinic in the Royal Victoria Hospital, Montreal.

5.1 Protocol

For phase I clinical trials, it is important to gather data as “pure” as possible, meaning that patient eligibility criteria should be strict. PEM subjects are women older than 18 years of age, non diabetic, non pregnant, who have had no previous surgery, chemotherapy or radiotherapy, and who have recently been diagnosed with a suspicious mass in the breast (from mammography or clinical examination). PEM scans are performed before the patients undergo biopsy, i.e., before the final histopathologic diagnosis of the tumour (benign or malignant) is known. Therefore, PEM classification (positive or negative) of the scan is done blindly.

Patients are asked to fast for at least 4 hours before the study, so that the glucose level in the blood is low [62][63]. The patient is then injected with 75 MBq of ^{18}F -FDG. Tumour cells, starved from patient fasting, will absorb the radioactive glucose available in the blood. Patients are encouraged to void before scanning, in order to decrease the amount of radiation dose to the bladder. The scan is performed at least 45 minutes after injection. FDG concentration in tissues is then supposed to have reached a plateau. This delay, which is used in most PET oncology studies, was chosen on the basis of brain studies, and its relevance to breast imaging will be discussed later.

5.2 Procedure

The PEM scanner is integrated into the Philips Mammo DIAGNOSTIC-UC mammography unit. Patients are scanned seated, with breast resting on the magnification table of the scanner, this table itself being fixed to the tray of the unit. This approach is used to acquire either x-ray mammograms or PEM scans without moving the patient.

Breasts are scanned separately. The breast in which a suspicious lesion was seen by x-ray mammography is called the “suspicious” breast. The other one is the “contralateral” breast. The suspicious breast is imaged first, so that the patient may be repositioned if the tumour is not in the useful field of view (5.9 cm x 4.9 cm) of the scanner. For each position, an x-ray mammogram is acquired in order to visualize the position of the tumour and to decide whether a PEM scan should be performed or the patient breast should be moved. The time required for a PEM acquisition is of the order of 5 minutes. When a satisfactory view of the suspicious breast has been obtained, the contralateral breast is imaged to allow comparison.

5.3 Decision making for diagnosis

When the PEM project was initiated, it was believed that malignant tumours (with high metabolic activity) would appear on the image as a “hot” (bright) spot compared with low activity healthy tissues (“background” of the tumour). On the other hand, benign tumours would not contrast with the background. Diagnosis was made easier by drawing profiles of activities through the image. A minimum 2:1 hot spot-to-background ratio was taken as indicative of cancer. Patient on figure 5.1 was declared “positive” (with cancer). On figure 5.3, the patient was “negative” (no cancer).

The PEM diagnoses were jointly made by K. Murthy, C.J. Thompson and Dr. R. Lisbona, the nuclear medicine physician who is a collaborator on this project. This decision-making procedure has obviously evolved with a better knowledge of the strengths and weaknesses of the instrument.

X-ray mammography diagnoses of the PEM patients were made by experienced radiologists, after observation of the microcalcification pattern of the tumour.

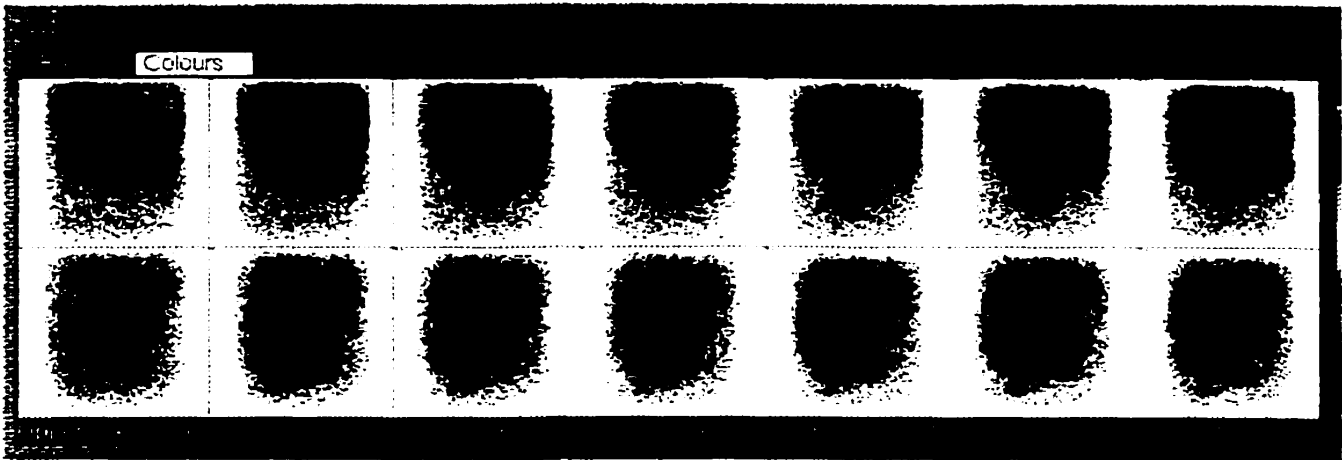


Figure 5.1: patient with cancer (“true positive”). The top image is the “suspicious” breast, the bottom image is the contralateral one. The tumour appeared as a hot spot in the suspicious breast.

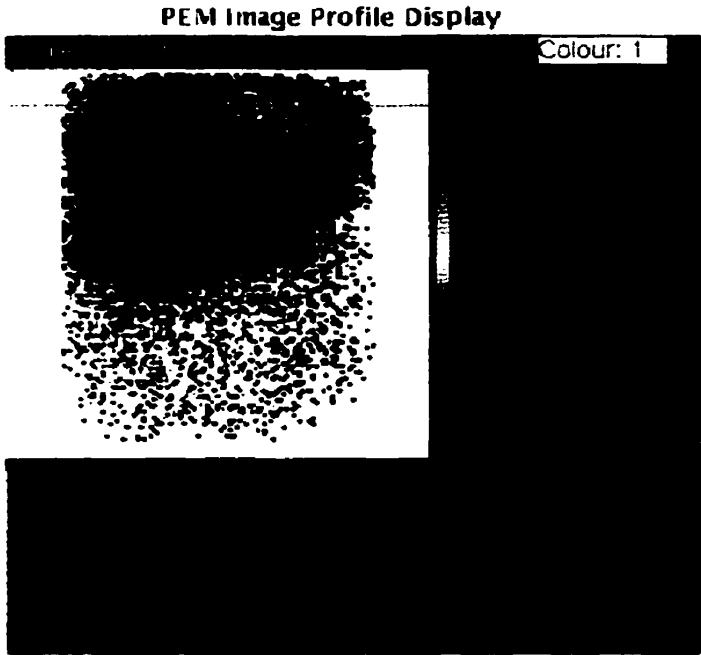


Figure 5.2 : profile through a hot spot.

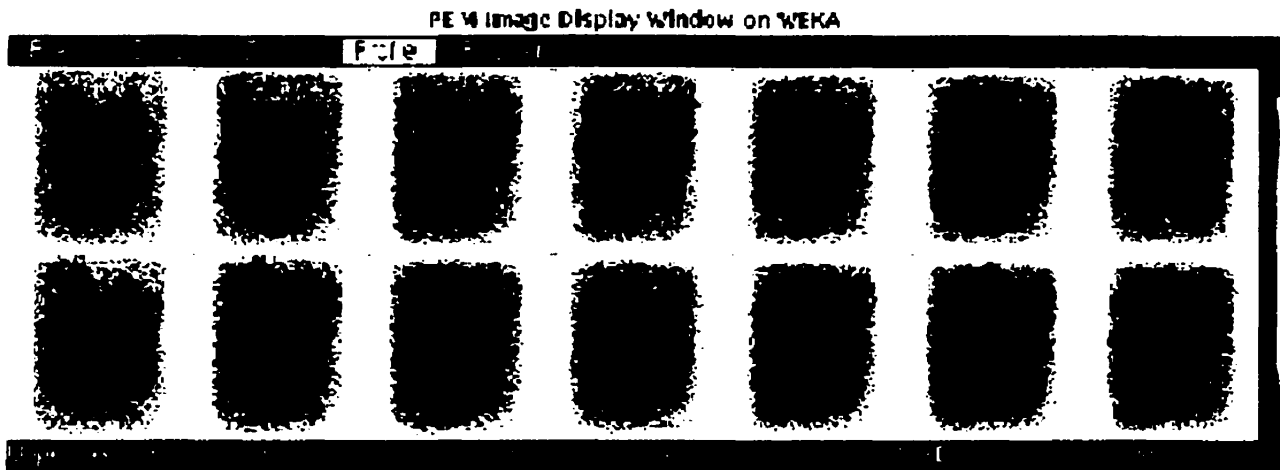


Figure 5.3: TRUE NEGATIVE. PEM images of this patient showed no hot spot. The tumour turned out to be benign upon biopsy.

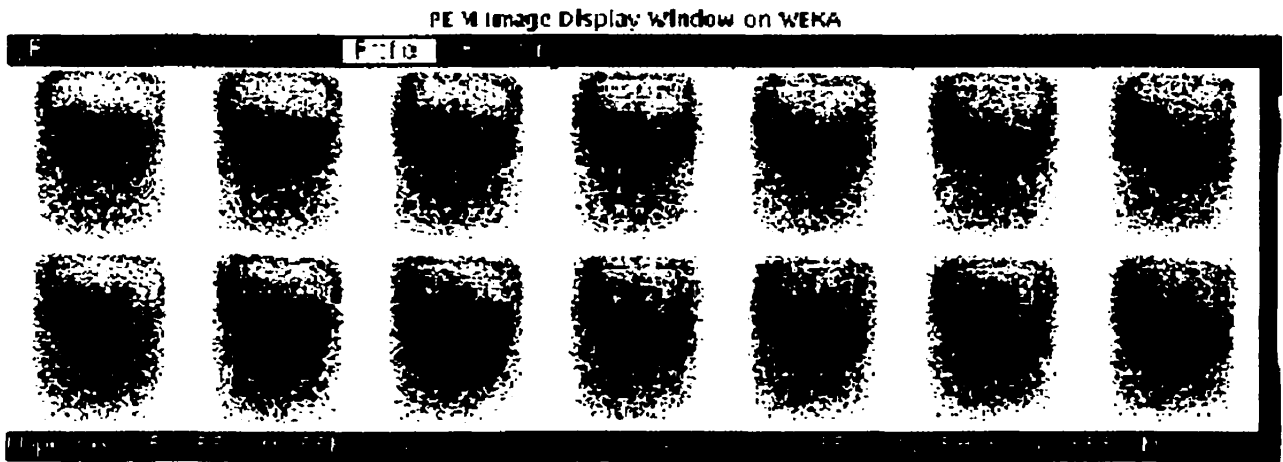


Figure 5.4 : FALSE NEGATIVE. No hot spot is seen, and this patient was diagnosed "negative" (no cancer) by PEM. However, upon biopsy, the tumour turned out to be an invasive ductal carcinoma grade 3.

5.4 Preliminary results

Within two weeks after the PEM studies, patients undergo surgical biopsy. Cytology then gives the final, incontestable diagnosis. When PEM diagnosis and cytology agree, scans are classified as being “true”, while a disagreement ensues “false” PEM scans. Hence, a patient who is referred to as a “true positive” had cancer and a positive PEM scan. A “false negative” (see figure 5.4) on the other hand, had cancer but a negative PEM scan.

Results are presented in table 5.1. Out of 15 patients scanned, 14 were eligible for PEM. One patient was treated for leukemia and no FDG uptake was shown, since treatments (such as chemotherapy or radiotherapy) interfere with metabolism.

Among these 14 eligible patients:

10 actually had cancer (all cases were invasive ductal carcinomas): PEM scans showed a hot spot for only 5 of them.. The histological grade of the missed tumours ranged from 1 to 3 and the smallest one was 1.1 x 1.1 x 0.9 cm. The true positive tumours had a grade 2 or 3, and the smallest size was 1.5 x 1.5 x 1 cm.

4 had a benign tumour: no hot spot was observed in any of these cases.

Thus, PEM results included 5 True Positives (TP), 4 True Negatives (TN), 5 False Negatives (FN) and no False Positive (FP).

Table 5.1: Preliminary results from PEM Patient Studies

Patient	X-ray Mammography	PEM	Cytology	Histological grade
1	+	-	-	NA
2	-	-	+	3
3	+	+	+	2
4	+	technical problems	+	1
5	+	+	+	3
6	+	-	+	2
7	+	+	+	3
8	+	-	-	NA
9	+	+	+	2
10	-	-	-	NA
11	+	+	+	3
12	+	-	+	2
13	+	-	-	NA
14	+	-	+	1
15	-	-	+	2

The diagnostic abilities of an imaging modality are usually described by three parameters, namely the sensitivity, the specificity and the accuracy, defined as follows:

$$\text{sensitivity} = \frac{\text{number of True Positive decisions}}{\text{actually positive cases}}$$

$$\text{specificity} = \frac{\text{number of True Negative decisions}}{\text{actually negative cases}}$$

$$\text{accuracy} = \frac{\text{TP} + \text{TN}}{\text{number of cases}}$$

The results for PEM and mammography are summarized in table 5.2.

Table 5.2: comparison between PEM and x-ray mammography

Modality	Sensitivity	Specificity	Accuracy
PEM	50%	100%	64%
x-ray mammography	80%	25%	64%

Low sensitivity of PEM was a serious concern and steps were taken to better understand why 5 malignant tumours had been diagnosed as benign. The initial explanation was related to the fact that

these tumours may have been out of the FOV when images were acquired. In fact, tumours that are close to the patient's chest wall do not fall within the FOV: tests have shown that the tumour must be at least 3 cm from the chest wall.

This is due to three factors:

first, the 2-cm space between the wall of the magnification table and the lower detector box, that can be addressed by redesigning the mechanical structure of the scanner or using oblique LORs,

second, the fact that the useful area of the PMTs is smaller than their actual surface: this requires a big investment in terms of new PMTs,

third, the 1cm lead shielding of the magnification table that prevents radiation from the heart from reaching the FOV. This problem could be solved by shielding the magnification table with a thinner layer of higher density material, such as tungsten, instead of lead.

The project of quantitation of PEM images began in that period, where it was crucial to understand which factors caused the false negative diagnoses.

CHAPTER 6.

Quantitative analysis of the data

6.1 Compartmental model

The role of quantitation in oncology PET is to assess the activity uptake of the tumour with respect to the activity uptake of the background. The first quantitative PET studies were done in the late 1970s by Sokoloff et al [64]. In order to calculate the local cerebral metabolic rate of glucose in rats and monkeys, they developed a compartmental model which mathematically described the behaviour of deoxyglucose in tissues. This model was later adapted to FDG uptake[65]. The detailed procedure is beyond the scope of this thesis, but the principles are briefly described below for completeness.

When a subject is scanned after FDG injection, two sets of data are acquired. First, arterial or venous blood samples are taken at gradually increasing time intervals. Blood sampling is used to draw curves of plasma glucose concentration and plasma FDG concentration. Second, a large number of PET images is acquired, in order to estimate the total amount of ^{18}F activity in a local region as a function of time.

These data are used to calculate four rate constants (k_1, k_2, k_3 and k_4), which are defined in figure 6.1. The metabolic rate of glucose can finally be determined using these rate constants and a “lumped constant”, which accounts for the differences in transport and phosphorylation between FDG and glucose.

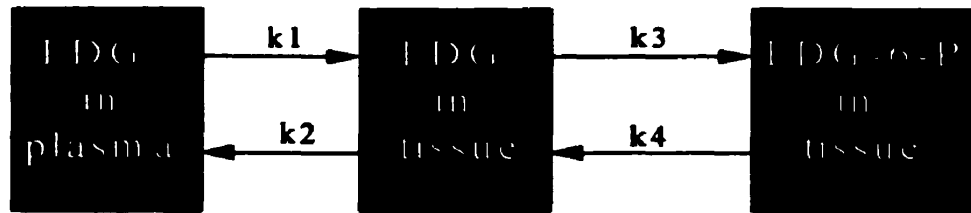


Figure 6.1: compartmental model describing the transport and phosphorylation of FDG.

From left to right, the three compartments respectively represent vascular space for FDG, tissue space for “free” FDG, and tissue space for FDG-6-phosphate.

k_1 is the rate constant for FDG transport from plasma to tissue.

k_2 is the rate constant for FDG transport from tissue back to plasma.

k_3 is the rate constant for phosphorylation of FDG to FDG-6-phosphate.

k_4 is the rate constant for de-phosphorylation, which is often considered to be negligible.

This approach is called “dynamic imaging”, and is the most detailed form of quantitative analysis. However, compartmental modelling is complex and time consuming. It cannot be incorporated into a routine screening procedure. Therefore, simplified approaches have been sought to evaluate the rate of glucose metabolism.

6.2 Standardized Uptake Value

Semi-quantitative analysis can be obtained from single-points measurements. The ratio of lesion activity to the injected dose is expressed as “Standardized Uptake Value” (SUV) or “Dose Uptake Ratio” (DUR).

However, SUVs are not “standardized”, in spite of their name, and almost each research

group has a different way of calculating them. Broadly, the SUV method consists of drawing a Region of Interest (ROI) including the tumour and estimating the number of counts detected from this region. The general formula is given by [63]:

$$SUV = \frac{\text{radioactivity concentration in ROI (Bq / ml)}}{\text{activity injected (Bq)/lean body mass (kg)}} \times \text{calibration factor} \quad (\text{Eq. 6.1})$$

The calibration factor takes into account scanner efficiency and other calibration parameters.

The “lean body mass” is considered instead of body weight in order to take into account the fact that fat absorbs much less glucose (or FDG) than functional tissues [66]. The lean body mass in kilograms may be calculated as follows [67]:

$$LBM = 45.5 + 0.91 \times [\text{patient height (cm)} - 152] \quad (\text{Eq. 6.2})$$

The drawbacks of the SUV method for quantitation are listed in references [68][69]:

- 1) many papers dealing with SUVs do not use lean body mass (or equivalent “body surface area”) correction.
- 2) the delay between FDG injection and PET scanning, although it has a very strong influence on SUV, is not standardized and sometimes not even mentioned (this effect will be discussed later)
- 3) precise plasma glucose measurements should be obtained before FDG injection (since presence of natural sugar in the blood can impair FDG uptake) and measurements corrected in consequence
- 4) partial volume effects (when ROI contains part of one anatomic structure and part of another) are not considered. Partial volume effects decrease with improved spatial resolution of the scanner.

Despite all these considerations, SUVs are often used in papers as conclusive information and may be interpreted without caution.

For this reason, until a standard procedure has been rigorously established, we chose not to express quantitative information in terms of SUV. Actually, we decided to rely solely on the activity difference between suspicious breast and contralateral breast. Since bilaterality (cancer in both breasts) occurs in less than 5% of cancers [70], and this feature is more likely to appear when the disease has reached an advanced stage, it is believed that asymmetry could be a valuable tool in early-stage screening.

Although this approach would not eliminate all the precautions required for SUV calculation, it would be more reliable than current quantification methods and could be interpreted more easily.

6.3 Retroactive correction

Because of the shortage of new patients (mainly due to restructurations at the Cedar Breast Clinic), it seemed interesting to use the data from previously acquired scans, even though they only aimed at hot spot observation. Several correction factors needed to be applied retroactively since no specific precaution was taken to facilitate comparison of both breasts, .

a) breast parameters

- size of breast

In practice, when the suspicious breast is scanned, technicians try to put as much breast tissue as possible within the field of view of the scanner. However, for the contralateral breast, they try to make it more comfortable to the patient, especially if she is small-breasted. As a result, little tissue is actually scanned (figure 6.2). To correct for this effect, a MATLAB program was written in order to convert the PEM image into a binary (black and white) matrix, and to calculate the fraction of the field of view covered by the breast.

PEM Image Display Window on WEKA

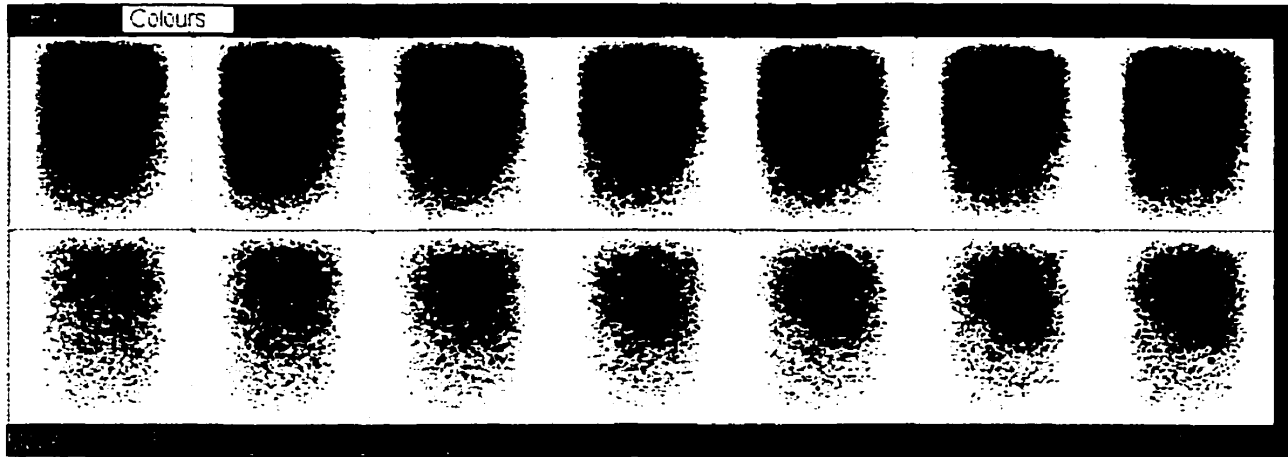


Figure 6.2: example of problem due to scanning parameters. The contralateral breast (bottom) was scanned for a shorter time, and less tissue was drawn into the FOV.

- compression

For the same reasons (more tissue in the FOV for suspicious breast), the compression used was often larger than for the contralateral breast. Though it is far from perfect, the easiest way to correct for this effect was to divide by the equivalent breast thickness over the field of view.

b) patient parameters

- glucose blood level

The presence of natural (not radioactively-labelled) glucose in the blood can seriously affect the results: indeed, proportionally, cells will absorb a lower fraction of FDG if natural glucose is also present [63]. Hence, image contrast will be reduced and diagnosis impaired. Some authors [71] suggest drawing blood before injection and to use a mean proportional correction. Unfortunately, since this procedure is not required for hot spot observation, only the last 3 patients in the series of 15 had their blood glucose level measured. The 4-hour fasting period prior to scanning reduces the risk of a high blood glucose level, but some differences are still observed from patient to patient. This correction will be applied in future quantitative studies.

- lean body mass

In our case, since the results are expressed in terms of percentage difference between both breasts, we chose not to apply this correction. Indeed, it is not likely that there will be a significant difference in tissue composition of the suspicious breast and the contralateral one.

c) physical parameters

- source decay

If several views of the breast are acquired in order to find the best imaging position, the time difference between the first suspicious PEM scan and the contralateral scan can reach up to 20-25 minutes. Therefore, the decay of the source should be accounted for when comparing 2 scans.

As discussed previously, once phosphorylated, FDG exits the cell at a very low rate. In most dynamic studies, the de-phosphorylation rate is neglected ($k_4 \sim 0$), since in healthy cerebral tissues, the typical (k_4) is always at least one order of magnitude smaller than k_1 , k_2 and k_3 [72]. Similarly, in this study, the biological clearance of FDG between injection and PEM scans will be neglected as well.

- efficiency (detector separation)

This factor is related to compression: when more tissue is drawn into the FOV and the compression is higher, the detectors will be further apart and detection efficiency will be lower (see figure 6.3). The efficiency was experimentally measured using several breast phantom with different heights. The detector separation was adapted to each phantom height in order to mimic the clinical conditions as closely as possible: the “top of phantom”- to-detector distance was equal to the “breast tissue”-to-detector distance due to the presence of the compression paddle during the clinical studies. The phantoms were filled with a ^{18}F -FDG water solution, with low activity (approximately 200 Bq/ml). The range of compression used covered all the compressions used in the clinical scans. A rough curve was obtained considering the four different phantom heights used and keeping in mind that the efficiency should approximately follow an inverse square law trend.

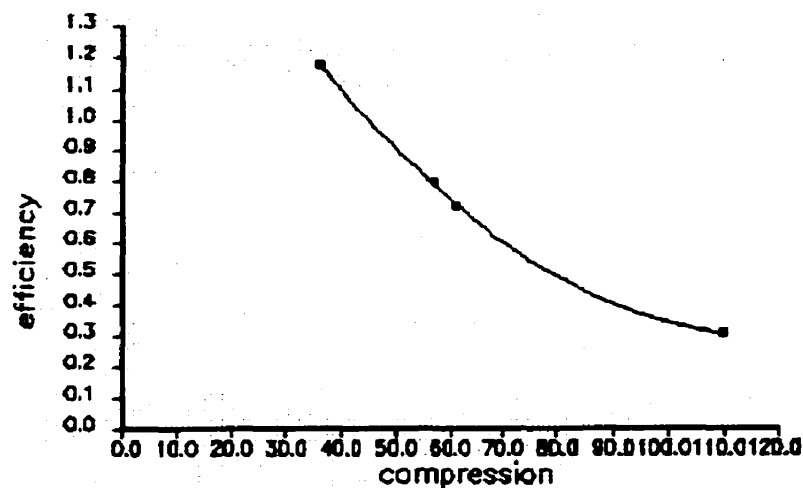


Figure 6.3: relative efficiency (normalized to a compression of 40) of the detectors versus breast thickness under compression (in mm)

Due to the limited access to ^{18}F -FDG for phantom experiments, it was not possible to repeat this experiment in order to provide some error bars. The data from figure 6.3 were then applied as a rough correction the clinical scans that were analyzed retroactively. However, this stressed the necessity to pay attention that the same compression be applied to both breasts for future clinical scans.

Considering the high spatial resolution of the PEM-1 scanner (~ 2.5 mm) and the size of the tumours (> 1 cm), it was decided not to account for partial volume effects.

6.4 Asymmetry calculations

The formula applied for each breast was then:

$$C_N = \frac{C_A}{t \times D \times S \times \eta} \quad (\text{Eq. 6.3})$$

where C_N represents the normalized number of counts in the breast

C_A is the number of accepted counts in the breast as displayed by the PEM program

t is the duration of the scan

η is the efficiency factor as taken from figure 6.3

D is the thickness of the compressed breast

S is the fraction of the FOV occupied by breast tissue as given by the MATLAB program

In the case of the contralateral breast, a factor accounting for the decay of the source between suspicious and contralateral scans is added.

$$C_{N(\text{contralateral breast})} = C_{N(\text{contralateral breast, not corrected for decay})} \times e^{-\frac{\ln 2 \times \delta t}{110}}$$

(Eq. 6.4)

where δt (in minutes) is the difference between the time at which the suspicious scan was performed and the time at which the contralateral scan was. The value of 110 minutes is the half-life of ^{18}F . The asymmetry percentage is then obtained by as follows:

$$A(\%) = \frac{C_{N(\text{suspicious breast})} - C_{N(\text{contralateral breast})}}{C_{N(\text{contralateral breast})}} \times 100 \quad (\text{Eq. 6.5})$$

6.5 Statistical analysis

The asymmetry threshold at which the separation between positive and negative scans would be drawn was decided on the basis of “receiver operating characteristic” (ROC) curve analysis [73], which is the recognized method for evaluating and comparing the diagnostic ability of medical imaging devices. True Positive fractions (TP/ actually positive cases) and False Positive fractions (FP/ actually negative cases) were calculated for every possible threshold (see figure 6.4). A 10% threshold was then selected in order to optimize the TP-to-FP ratio.

In fact, an 8% threshold results in improved sensitivity. However, the value of 10% was chosen because, in the series of data from this study, sensitivity is not affected by varying the threshold between 10 and 15% (all count asymmetry percentages are either below 10% or above 15%). Therefore, it is more reliable to draw the line between positive and negative diagnoses at a 10% threshold.

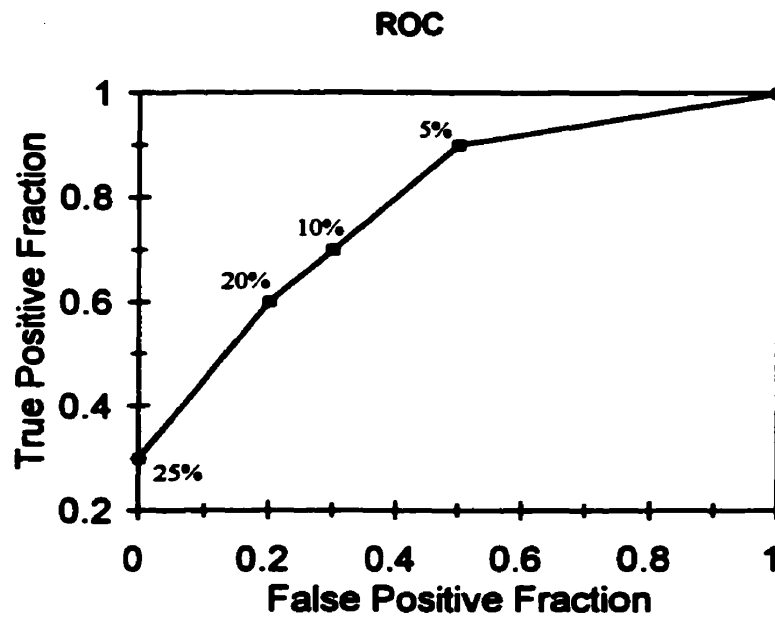


Figure 6.4: ROC curve.

6.6 Results

Count asymmetry for all 14 scanned patients ranged from -21% to 53%. Negative patients all had percentage differences below 6%.

3 out of 5 false negatives showed more than 10% asymmetry. In 2 cases, 40-50% asymmetry was observed. Because different imaging parameters were used for contralateral and suspicious breasts, this activity difference was not visible directly on the images. Table 6.1 summarizes the differences in compression, scanning times, delay between scans that could explain the false diagnoses.

Table 6.1: results from count asymmetry and critical scanning parameters

Patient	PEM diagnosis	Asymmetry	Compression difference (in mm)	Time between injection and susp. scan	Time between susp. and cont. scans
1	TN	6 %	0	70	8
2	TP (A)	43 %	0	54	8
3	TP (HS +A)	21 %	9	49	17
4	tech	tech			
5	TP (HS+A)	17 %	5	42	24
6	TP (A)	22 %	12	53	18
7	TP (HS)	0 %	15	44	8
8	TN	- 4 %	0	81	20
9	TP (HS +A)	51 %	0	60	17
10	TN	2 %	15	35	7
11	TP (HS)	9 %	10	59	11
12 bilateral	FN	- 13 %	16	72	30
13	TN	- 21 %	7	62	13
14	FN	8 %	18	72	9
15	TP (A)	53 %	22	74	7

This table also shows the new classification of diagnoses (true positive, true negative or false negative) when both hot spot observation (HS) and count asymmetry (A) are taken into account. In this case, the diagnostic characteristics of the PEM scanner are sensitivity = 80%, specificity = 100%, accuracy = 86%.

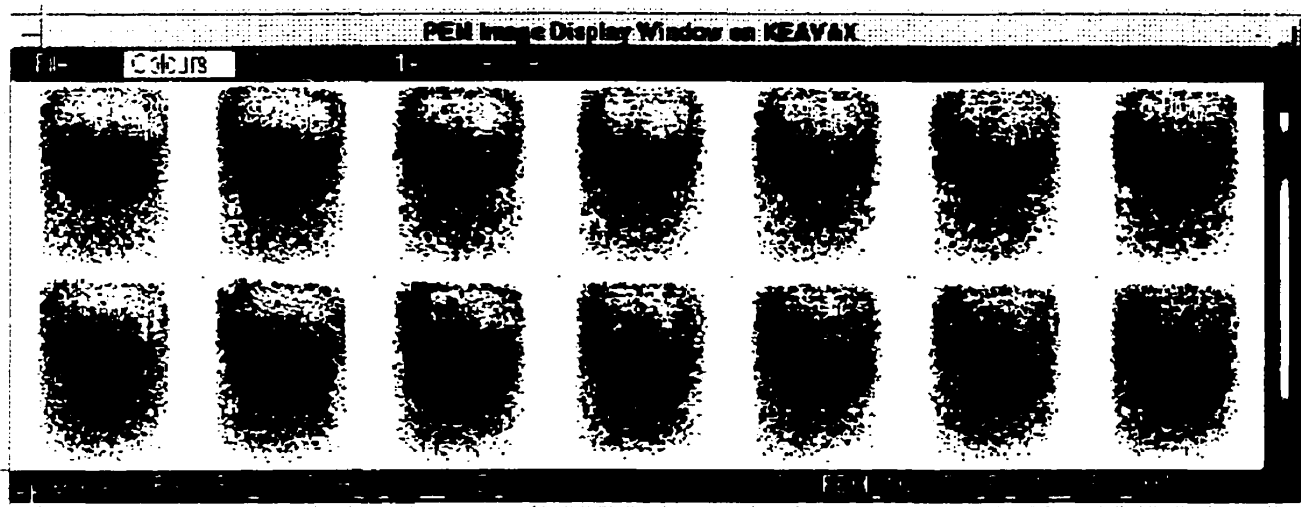
Corrections for scanning duration and source decay are straightforward. However, it is very difficult to correct retroactively for compression and detector separation: it would require an experiment that mimics perfectly the clinical conditions (flexible phantom, with compressible tumours of different sizes . . . etc.). Unfortunately, retroactive corrections cannot completely make up for the loss of information that happened during patient scanning. For example, one of the remaining false negatives (8% asymmetry, compression difference being one of the highest) may turned positive if corrections could be perfectly applied.

There is possibility of one false positive, in which the contralateral breast shows 21% more counts than the suspicious one.

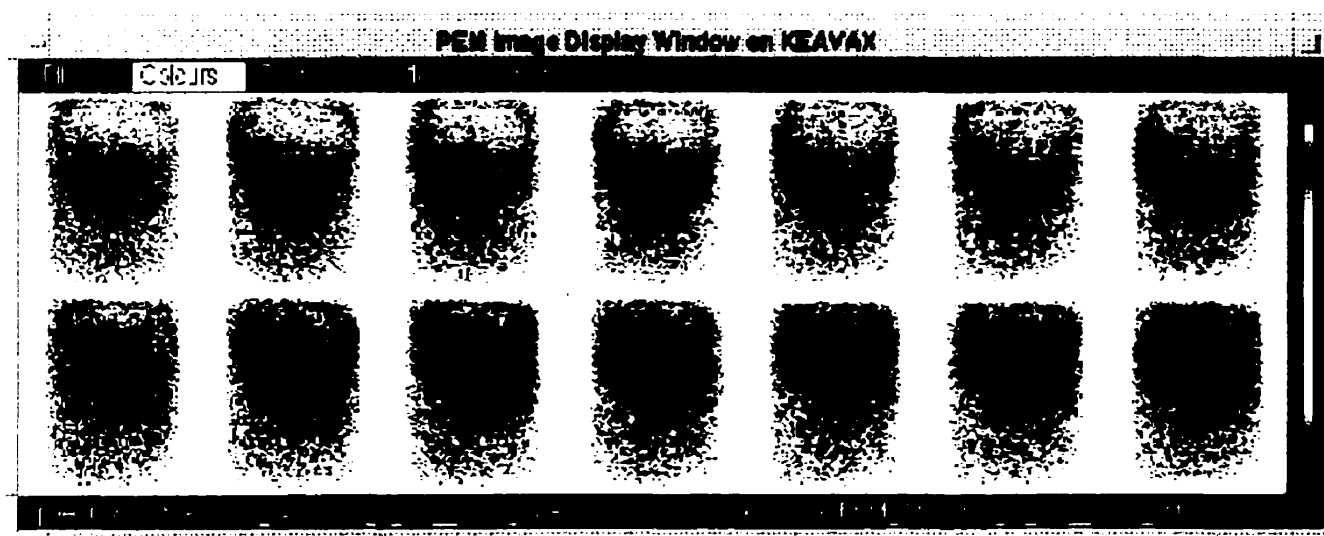
6.7 Programming

To examine the effect of the different scanning parameters on the final image, the PEM display program was modified to apply the correction factors listed above and to display corrected images. These modifications implied writing three new Fortran subroutines to extract the needed information in the LIST files where it was stored.

As a result, some corrected false-negatives now clearly appear to be positive on the computer screen (figure 6.5) while true negatives stay negative (figure 6.6) and true positive stay positive (figure 6.7). Again, though this cannot be used to correct diagnoses that have already been made, it stresses the fact that scanning parameters have a crucial influence on the images and that no decision can be taken by comparing both breasts if they are not rigorously identical.

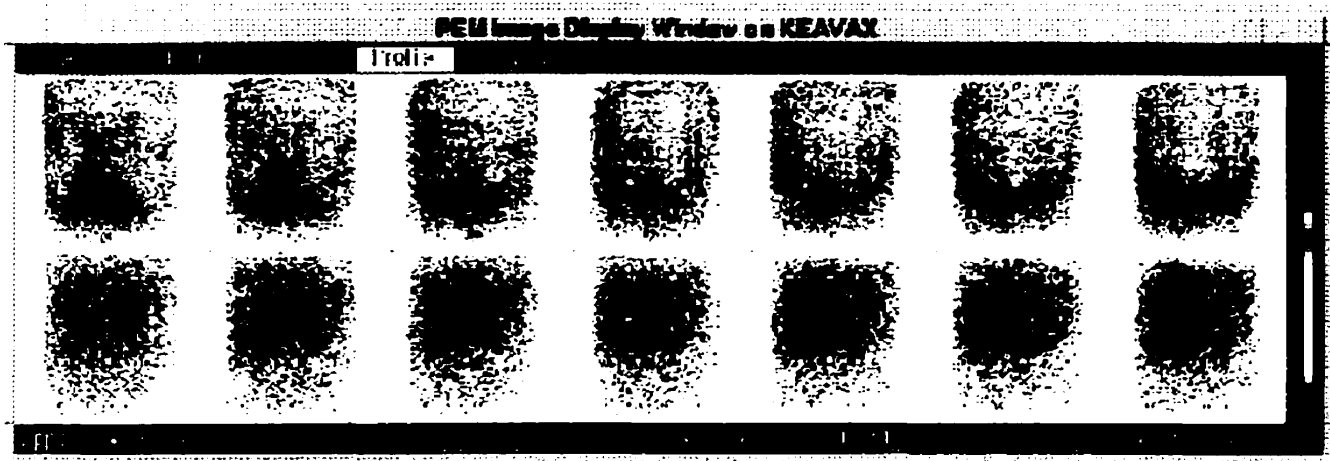


A) images were acquired with different scanning parameters. Contralateral and suspicious breasts seem to have uptaken the same amount of activity. The patient was then diagnosed as "negative".

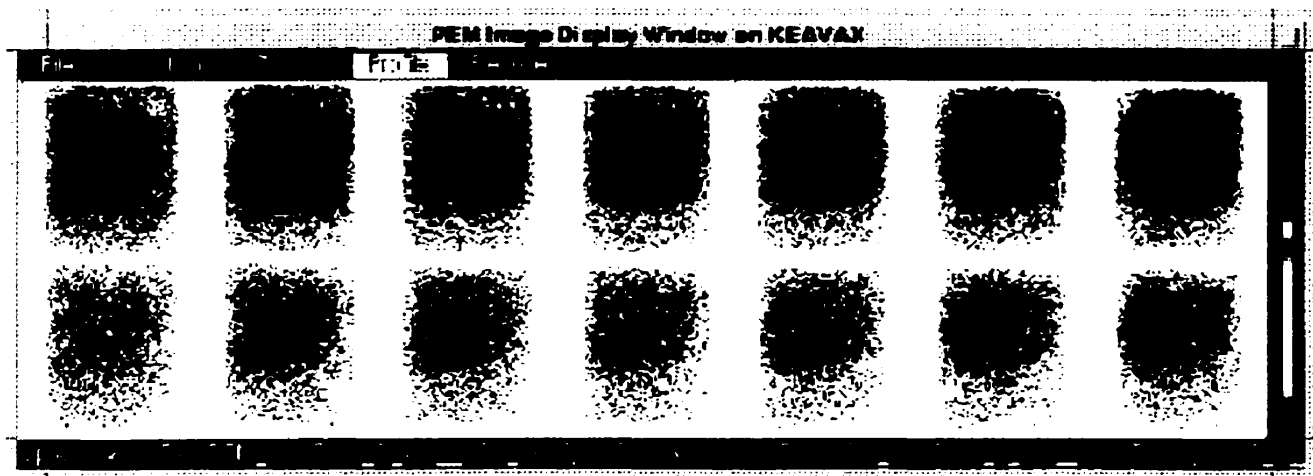


B) images are corrected in order to cancel the differences due to scanning parameters. The suspicious breast (top) appears to be more active than the contralateral breast (bottom) is. The patient had a grade 3 carcinoma.

Figure 6.5: images of a patient that was first diagnosed negative. A) without quantitative correction, B) with correction.

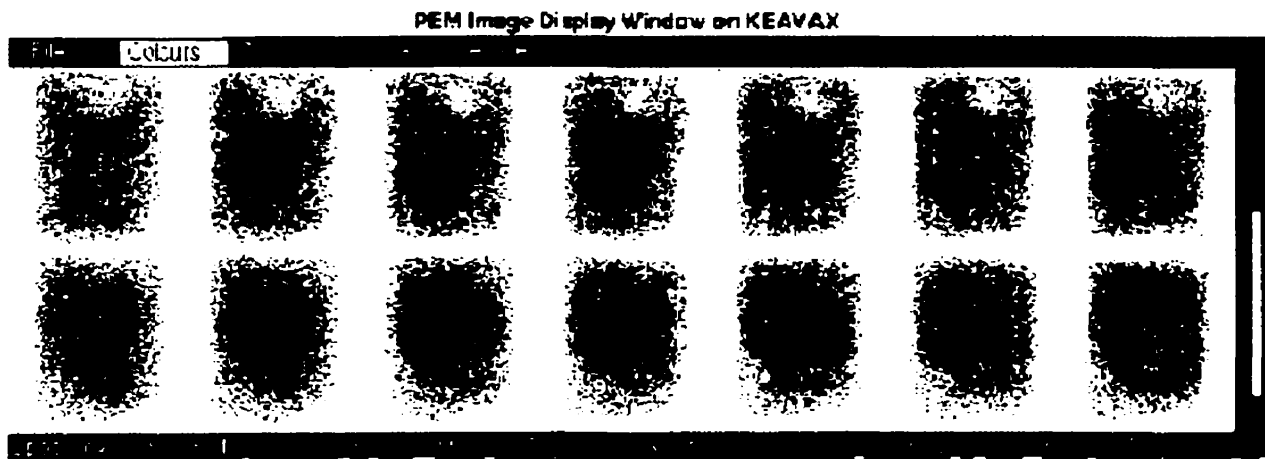


A) true negative images without correction for scanning parameters. The suspicious breast (top) seems to have higher activity.

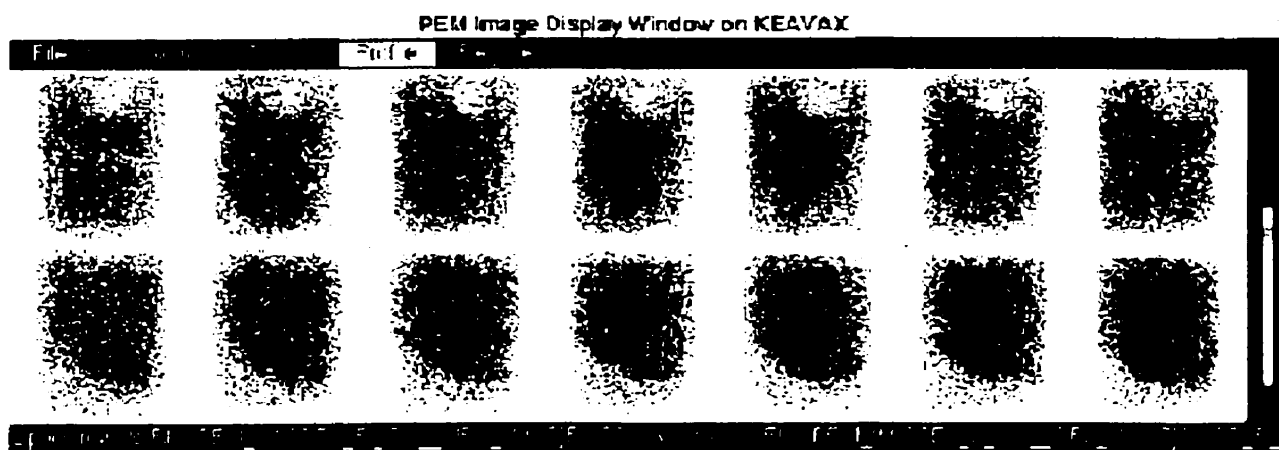


B) true negative images of the same patient after correction. The activity in the suspicious breast looks lower than in image A.

Figure 6.6: Effect of quantitative correction on the images of a true negative patient. A) without correction, B) with correction.



A) true positive images without correction: a hot spot is visible in the suspicious breast image.



B) true positive images with correction for scanning parameters. The contralateral breast (bottom) appears slightly less active than in image A.

Figure 6.7: True positive images A) without quantitative correction, B) with correction.

CHAPTER 7.

Parameters affecting PEM images

7.1 Contrast resolution

Contrast resolution of a nuclear imaging instrument describes the ability of the system to identify areas of increased radio-tracer uptake against areas containing background radioactivity. To assess as accurately as possible the characteristics of the PEM-1 scanner in terms of contrast, we used wall-less hot spots according to the method developed by Kavita Murthy [74]. These hot spots are made by mixing a radioactive solution with a heated agarose solution. The resulting mixture can be poured into a plastic mould of any shape. When hot, this mixture is liquid but upon cooling, it sets to a gel and can be separated from the mould. This technique is very cost-effective (only 25 mg of agarose powder are needed per millilitre of water) and offers the advantage of eliminating the non radioactive wall of conventional hot spots, which by its very presence can impair image contrast.

In these experiments, we used spherical moulds to produce 12 mm and 16 mm diameter hot spots. They were placed in a custom made plexiglass breast phantom containing water at room temperature with various amounts of background activity. After 30 minutes, leakage of activity from a newly-made hot spot into a non-agitated background was found to be less than 0.1% of total hot spot activity.

Contrast resolution is related to “true contrast”, “projection contrast” and “image contrast”.

The true contrast (C_{true}) is the ratio of the known activity per gram of the tumour (simulated

by the hot spot) to that of the background. The projection contrast (C_{proj}) is defined as the ideal contrast “seen” by the detectors in a projection image. In planar geometry (shown in figure 7.1), for a spherical tumour of diameter D and specific activity A_{HS} , in a background of thickness T and specific activity $A_{background}$, C_{proj} and C_{true} are given by:

$$C_{proj} = C_{true} \times \frac{D}{T - D} \quad (\text{Eq. 7.1})$$

$$C_{true} = \frac{A_{HS}}{A_{background}} \quad (\text{Eq. 7.2})$$

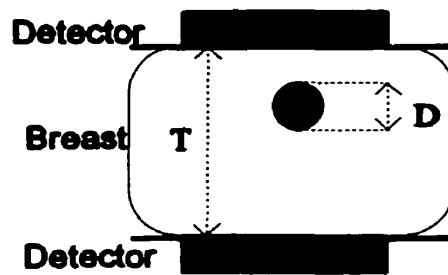


Figure 7.1: Planar geometry used to derive equation (7.1).

The image contrast (C_{PEM}) is the contrast as seen in the reconstructed final PEM image and is obtained by drawing profiles through the hot spot and the background. C_{PEM} is the ratio of counts in the peak of the hot-spot image profile and that in the background image profile.

The results are presented in figure 7.2, where C_{PEM} and C_{proj} are plotted versus C_{true} . The energy window was set as 350–650 keV. The detector separation used was within the range of typical compression values of the clinical scans (equivalent breast thickness = 70 mm). Experimental data agree well with predicted data C_{proj} for the 12 mm hot spot. The agreement seems to be poorer for the 16 mm hot spot, but this may only be due to the higher contrast range: for the 12 mm hot spot,

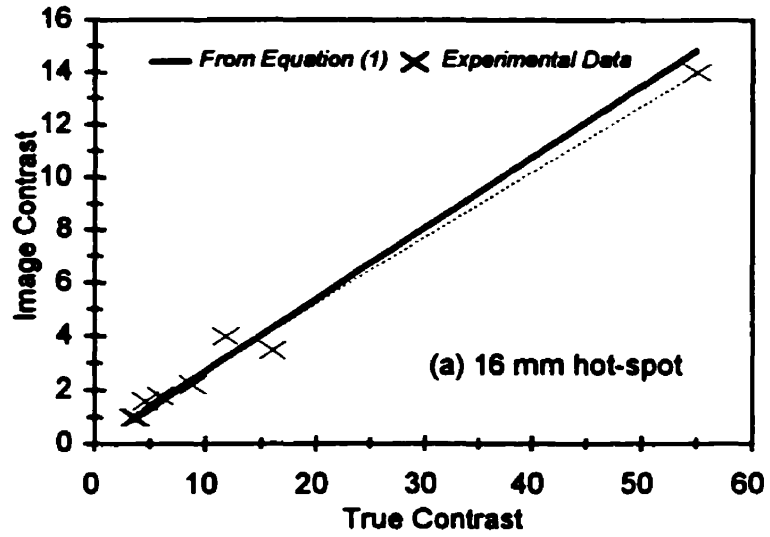
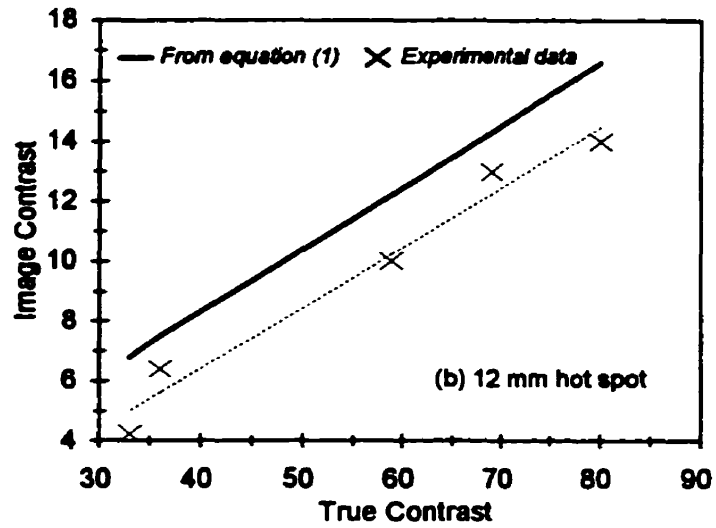


Figure 7.2 : results of contrast resolution experiments, for 12 mm and 16 mm diameter hot spots. Theoretical data were obtained from equation 1 (C_{proj}) and experimental data from image profiles (C_{PEM})

the true contrast varies between 0 and 60. Theoretical and experimental data start diverging for a true contrast of 30. Therefore, the range of true contrast for the 16 mm hot spot being 30 to 90, the divergent effect is more noticeable.

One conclusion of this experiment was that a true contrast (C_{true}) of 10:1 is necessary to produce a 2:1 image contrast (C_{PEM}). Images with lower true contrast cannot be accurately evaluated qualitatively. As discussed in section 5.3, for decision-making by hot-spot observation, a PEM image contrast of 2:1 or higher is required to diagnose the patient as with cancer.

Consequently, some malignant tumours may cause false-negative diagnoses, either because 1) they are too big or too small and offer a low image contrast (see figure 7.3) or 2) too diffuse to produce a real hot spot (the delimitation between tumour and background is unclear) or 3) because they have low FDG absorption compared with the majority of tumours and do not produce a sufficient image contrast. Quantitative comparison between both breasts bypasses this problem.

7.2 Dead time

Dead time, or pulse resolving time, is related to the time required to process individual detected events. If one coincidence occurs before the previous one has been completely processed and has disappeared from the crystals and electronics, the two signals will overlap and may be considered as an invalid event. The result is a loss of valid events, referred to as dead time losses. They can occur in the crystals, during event processing, or in the computer interface.

Most nuclear medicine imaging devices in are said to be “paralyzable” systems meaning that each event introduces a dead time τ whether or not that event was actually counted. The theoretical equation for paralyzable dead time [75] is:

$$R_o = \frac{R_t}{1 + R_t \times \tau} \quad (\text{Eq. 7.3})$$

where τ is the dead time, R_o is the observed count rate and R_t is the true count rate.

However, equation 7.3 cannot be applied to the PEM-1 system, because event acquisition is disabled

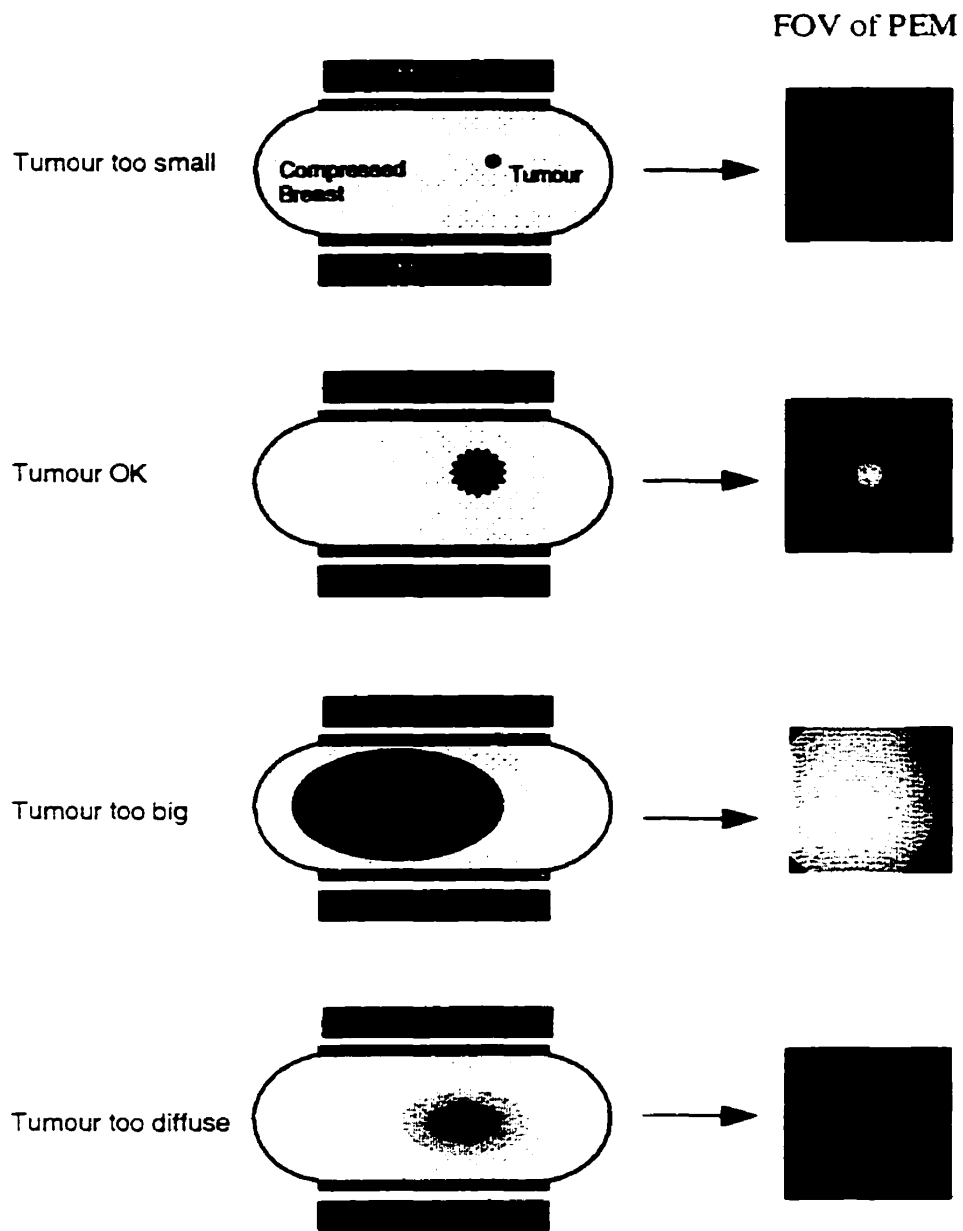


Figure 7.3: Different aspects of the PEM images depending on tumor size or structure. In cases 1,3 and 4, a hot spot is not observed.

for 4 ms every 1024 events while data transfer is taking place between the ADC and the computer interface. This is limitation imposed by the maximum buffer size of the ADC and has no relationship to the dead time as defined conventionally by equation 7.3. A better evaluation of the system performance is given by estimating the “live time” as a function of the input count rate. This was done by placing a point source in the centre of the FOV and by varying the separation between the detectors. Input count rates are measured at the input of the ADC. Output count rates are calculated from the number detected counts used to form the image.

In figure 7.4, the percentage of “live time”, i.e. the percentage of counts detected is plotted

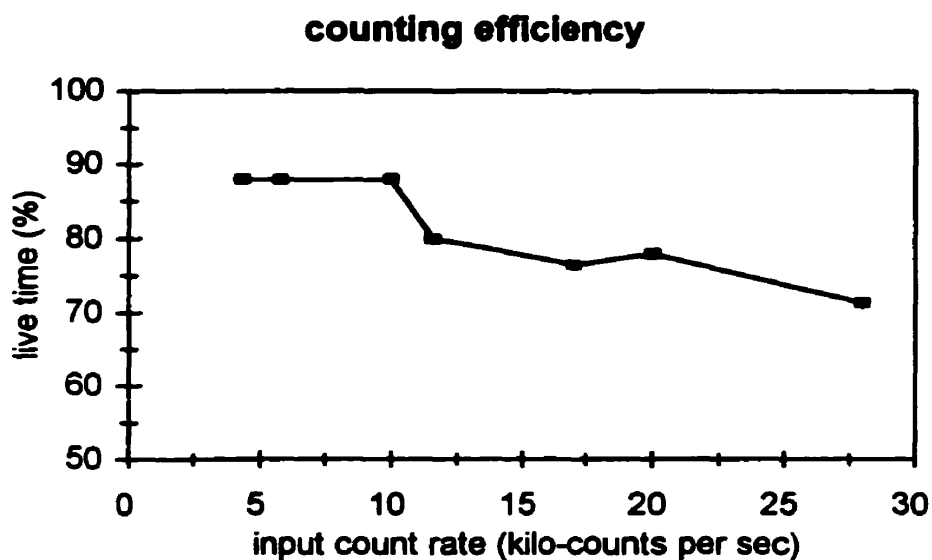


Figure 7.4: “live time” of the PEM-1 scanner

versus the input count rate. Even for high emitted count rates (of the order of 20 kilo-counts per second), about 75% of the input counts are detected by the PEM system. Hence, count losses are reasonably low, and breast images should not be significantly affected by this factor.

7.3 Radiation from the heart

FDG uptake by the heart is generally of the order of 3% of the injected dose [76]. In comparison, the uptake in one breast is less than 1%. For PEM patients injected with 75 MBq, heart uptake would then be 2.6 MBq. Despite the 1-cm thick lead shielding of the magnification table, the presence of the heart could reduce contrast in the breast image. Moreover, it cannot be determined if this amount of extraneous radiation would be of the same magnitude in both breasts.

In humans, the heart weighs roughly 300 grams and is located slightly left to the midline (~ 2/3 on the left side, 1/3 on the right) [77]. To study the effect of uptake in the heart on breast images, we placed a heart phantom of 300 ml and 2.6MBq activity at the appropriate location with respect to a breast phantom of 1200 ml with 0.6 MBq. A 16 mm 0.4 MBq hot spot was inserted in the breast phantom to mimic a malignant tumour.

In order to achieve a wide range of contrast values in a short period of time, the heart and breast phantoms were filled with an FDG solution, while the hot spot used ^{11}C as a positron emitter. It was then possible to let the hot spot activity decay while heart and breast activities remained relatively stable (half-life of ^{11}C is 20 minutes, while half-life of ^{18}F is 110 minutes).

Results are presented in figure 7.5, where C_{PEM} with and without the heart phantom are plotted versus C_{true} . The two sets of data agree reasonably well, although a small decrease in image contrast is seen when the heart is present.

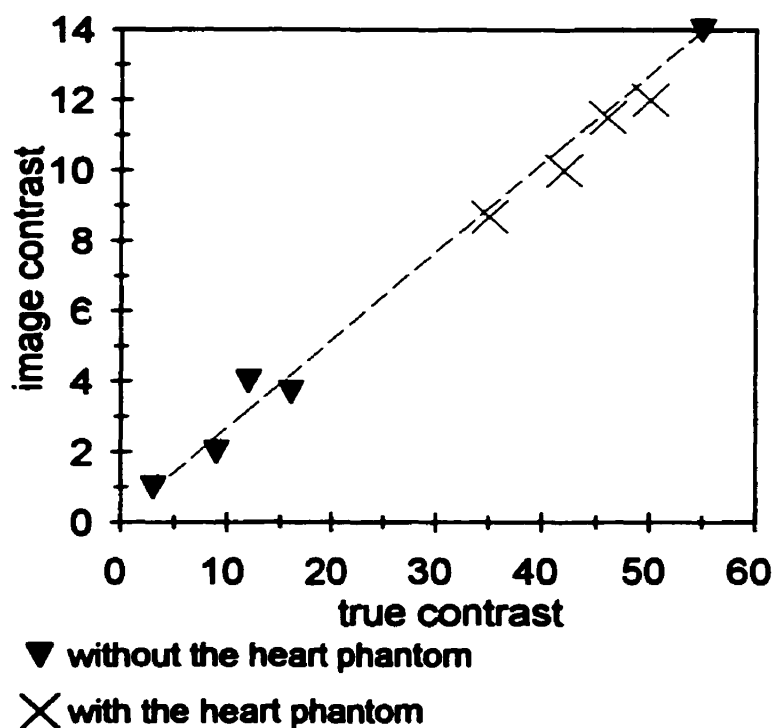


Figure 7.5: influence of radiation from the heart on image contrast.

In conclusion, no significant reduction of contrast due to the presence the heart was observed on the image. Thus, this parameter is not taken into account while applying quantitation to the right or the left breast.

7.4 Time interval between scans/ first scan and injection

The delay between FDG injection and the first scan has been chosen to be at least 45 minutes based on brain studies [64][78]. After 45 minutes, FDG absorption in normal brain tissue reaches a plateau and quantitation is meaningful. However, if this delay is not respected, quantitative data loses all significance, since a malignant tissue imaged at time t could exhibit the same activity as healthy

tissue imaged 15 minutes later. This 45 minute wait before scanning, sometimes extended to 60 minutes, has been widely accepted in oncological procedure.

Recent studies suggested that brain and other tissues, especially tumours, have dramatically different behaviours as far as FDG absorption is concerned. Hamberg et al [69][79] showed that the plateau may be reached only after 5 hours in patients with advanced-stage lung cancer. Figure 7.6 shows that the difference the “dose uptake ratio” or DUR (which is equivalent to SUV) at 60 minute post-injection and the plateau DUR is around 40% in non-treated tumours. Hamberg et al. stress the fact that since FDG uptake depends on the biology of every single tumour, the error associated to DUR calculation before the plateau is reached is unpredictable.

It is not clinically feasible to respect a 5-hour delay post-injection, since it would mean fasting the patient for at least 9 hours, and injecting almost 7 times more activity (500 MBq). Hence, the simplest solution may be to scan before the plateau is reached (in the rising portion of the curve) but always with the same delay with respect to injection (to allow comparison between patients). In that case, it would be crucial to keep contralateral and suspicious scans as close in time as possible in order to limit errors due to increased FDG absorption in the latest scan.

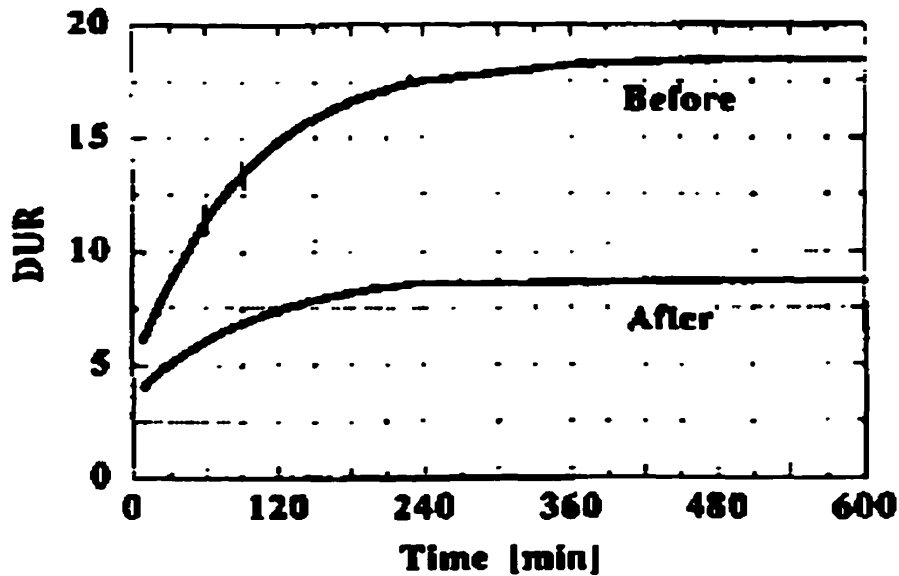


Figure 7.6: ^{18}F -FDG absorption, and hence DUR, keeps increasing with time for 5 hours after injection in untreated tumours ("Before"). The plateau is reached sooner in treated tumours ("After") [69].

The influence of this effect on image contrast (i.e., on hot spot observation) is not clear. However, the increasing FDG absorption can introduce significant errors in count asymmetry calculations. Moreover, it is not possible to correct retroactively for this effect if scans are separated by too long a time interval, since no standardized model is available for FDG uptake in tumours.

CHAPTER 8.

Discussion

8.1 Diagnostic improvement

Although count asymmetry demonstrated retroactively that PEM sensitivity was actually higher than previously calculated from hot spot observation alone, this method cannot be tested yet as a diagnostic procedure, since decision-making was no longer “blind” (we knew which patients had cancer). Indeed, some results appear very contradictory : a negative patient with 21% asymmetry, a positive patient with 0%... These cannot be explained but by the fact that some of the criteria discussed in chapters 6 and 7 were not respected. In the examples given above, the first patient (negative but 21 % asymmetry) was scanned with a long delay between suspicious and contralateral scans. The second patient (positive but 0 % asymmetry) was scanned with a short delay between injection and scans, and high compression difference between both breasts.

New patients would be needed to assess the value of PEM count asymmetry in breast cancer detection. One important point is that we are now aware that some tumours because of their size or fibrotic component, will not appear as a hot spot on PEM images and that the activity of the whole field of view should be considered.

Hopefully, if more attention is paid to allow a significant comparison between both breasts, sensitivity could be further increased.

8.2 Standard procedure

The study of the list files showed that the pitfall was more in the scanning procedure than in the device itself. Several problems were pointed out, and wrong diagnoses may have been caused by one or more of these during a single scanning procedure. To summarize, these issues were:

- 1. The delay between injection and scans was too short**
- 2. The compression was not the same for both breasts**
- 3. Not enough attention was paid in positioning and scanning of contralateral breast**
- 4. Different scan durations were used for both breasts**
- 5. The delays between suspicious scans and contralateral scans were too long**

Another point was raised about patient care between injection and scans: as discussed previously, FDG is not tumour specific, but is actually absorbed by any glucose-consuming tissue. It was suggested that, in order to avoid FDG accumulation in undesirable locations (i.e. the brain, or the ocular muscles) the patient should lie in a dark, quiet room in order to prevent noise and visual stimuli, should not walk to the scanning room but be carried in a wheel-chair . . . etc. Therefore, physical activity and conversation should be kept at a minimum.

The scanning procedure, including the new elements, will then be standardized as follows :

- 1. Make sure that patient has fasted for at least 4 hours**
- 2. Draw patient blood before injection and evaluate glucose level**
- 3. Inject patient with 75 MBq of ^{18}F -FDG**
- 4. As much as possible, keep patient away from light and noise. Ideally, she should be resting and lying down in a dark, quiet room.**
- 5. Wait at least 45 min (60 min would be better) between injection and first scan**
- 6. Take patient to the mammography room in a wheel chair**
- 7. Set all technical parameters (compression, scanning duration, amount of tissue drawn**

in the field of view) identical for both breasts

8. Keep delay between suspicious scan and contralateral scan as short as practically possible.

In cases where this step is too troublesome, one possibility would be to do one contralateral scan before the several suspicious scans, and another one after.

9. Diagnosis should be made by both looking at images and considering quantitative data

8.3 Correlation of asymmetry with tumour parameters

Obviously, “pure” data (i.e. conform to standard procedure) would be required to investigate correlation between PEM information and tumour characteristics. However, we can already think that the following correlations would be of interest:

asymmetry and grade (histological and nuclear)

asymmetry and stage

asymmetry and size of tumour

asymmetry and survival

So far, no correlation appears to be obvious (see table 8.1). In addition to the contamination of the data by the incorrect scanning parameters, it can be due to the fact that the pathology reports (describing the cytologic characteristics of the tumours after biopsy) were not standardized either. In some reports, the nuclear grade is clearly stated, and the several components of the tumour (fibrotic, medullary, in-situ vs invasive. . .) are detailed while in others, much less information is available. With the help of Dr. Manon Auger, director of Cytopathology in the Pathology Department at the Royal Victoria Hospital, some of this missing information was gathered. A standard procedure for pathology reports at the RVH has now been established. Of our interest for PEM studies, the proportion of in-situ versus invasive component in the tumour will now be stated.

These parameters could be studied with new patients and could help in better determining the potentials of the PEM-1 scanner.

Table 8.1: characteristics of patients' tumours

Patient number	Size of tumour (cm)	HG	NG	Tumour characteristics (as described in pathology report)	Asymmetry
2	1.1x1.1x0.9	3	3	invasive ductal carcinoma	43 %
3	1.5x1x1	2	3	invasive ductal carcinoma (with focal papillary component) in-situ component (papillary and cribriform types)	21 %
5	2.5x2.2x2.2 2x1.5x1.2	3	3	invasive ductal carcinoma in-situ carcinoma (solid and cribriform types)	17 %
6	5x3	2	2	in-situ and invasive ductal carcinoma	22 %
7	1.8x1.5x2.5	3	3	invasive ductal carcinoma	0 %
9	3x3x2 1.5x1.5x1.5 2x1.5x1.5	2	2	invasive ductal carcinoma invasive tubulo-lobular invasive tubulo-lobular	51 %
11	1.5x1.5x1.3	3	3	in-situ and invasive ductal carcinoma (fibrosis in centre)	9 %
14	2x1x4.5	1	1	invasive ductal carcinoma less than 5% in situ component (cribriform), fibrotic	8 %
15	1.2x1.0x1.2 0.8x0.8x0.8	2	2	invasive and in-situ ductal carcinoma invasive and in-situ ductal carcinoma	53 %

HG : Histological grade, NG : Nuclear grade

8.4 Potential of quantitative analysis for follow-up

The medical community expects a lot from quantitation of metabolic images. One of the main reason is the potential to compare between images of a patient at time of diagnosis and images of the patient after therapy. In the case of oncology PET, it would provide an estimate of the metabolic changes in the tumour in response to therapy (chemotherapy, radiation therapy, . . .) [80][81]. If the tumour exhibits no decrease in metabolic activity (i.e. decreased FDG uptake), another therapeutic modality should be chosen. This follow-up is already in use, but relies on anatomic images: a significant delay (which can be crucial in terms of patient survival) is required between changes in tumour metabolism and structural modifications.

In the case of PEM, because of the limited dose injected, patient follow-up could easily be done several times without interfering with the actual therapeutic procedure.

CONCLUSION

Positron Emission Mammography is a high-efficiency, high-specificity technique for breast cancer detection and staging. However, when diagnosis was performed based on hot spot observation alone, some malignant tumours were missed. These results suggest that breast carcinomas have different uptake behaviours with respect to FDG. Count asymmetry of PEM images offers a quantitative tool for diagnosis, and allows the detection of big or diffuse malignant tumours. Hence, the diagnostic decision-making based on both quantitative analysis and hot spot observation is more reliable than it used to be without quantitation: in this series of patients, the sensitivity of PEM-1 would be increased by 30% (from 50% to 80%), and the accuracy from 64% to 86%.

The integration of quantitative calculations into the PEM software will provide the user with almost 'live' information in future PEM scans. More clinical trials are required to assess the actual impact of the standardization of the scanning procedure and the application of quantitative analysis of the images, but a further improvement in PEM sensitivity can be expected.

In the near future, quantitative information will be a central part of patient follow-up studies, for the assessment of tumour response to therapy. In addition, count asymmetry will be useful if the PEM scanner is adapted to assess the involvement of axillary lymph nodes. Other expected PEM studies, such as the study of other radiopharmaceuticals (generator-produced), will also benefit from this method.

References

1. Parker SL, Tong T, Bolden S, Wingo PW. Cancer Statistics, 1997. *CA-A Cancer Journal for Clinicians*. 1997;45:5-27
2. National Cancer Institute of Canada: Canadian Cancer Statistics 1998, Toronto, Canada, 1998. (Official website : www.cancer.ca)
3. Canadian Cancer Society. Facts on Breast Cancer. *General free publication*
4. Couch FJ, DeShano ML, Blackwood MA, Calzone K et al. BRCA1 mutations in women attending clinics that evaluate the risk of breast cancer. *New England Journal of Medicine*. 1997; 336: 1409-1415.
5. Ries LAG, Kosary CL, Hankey BF, Miller BA. SEER Cancer Statistics Review 1973-1994: Tables and Graphs. Bethesda, MD: *National Cancer Institute*; 1997. NIH publication No. 97-2789.
6. Figure extracted from the American Cancer Society "Breast cancer resource center"'s website www3.cancer.org/cancerinfo/documents/overviews/breaover.asp?ct=5
7. Rosai J. Ackerman's Surgical Pathology. Seventh edition, volume 2. Ed : the CV Mosby company, 1989 St Louis, Missouri. 1216-1245.
8. National Coordinating Group for Breast Screening Pathology. Pathology Reporting in Breast Cancer 1995. *NHSBSP Publication no. 3*.
9. Bloom HJG, Richardson WW. Histological grading and prognosis in breast cancer. *British Journal of Cancer* 1957; 11:359-377.
10. Scarff RW, Torloni H. Histological typing of breast tumours (international histological classification of tumours no. 2). *Geneva: World health organization* 1968.
11. Elston CW, Ellis IO. Pathological prognostic factors in breast cancer. I. The value of histological grade in breast cancer: experience from a large study with long term follow-up. *Histopathology* 1991; 19: 403-410.
12. Hutter RV. At last—worldwide agreement on the staging of cancer. *Archives of Surgery* 1987; 122: 1235-1239.
13. Canadian Medical Association. Clinical Practice Guidelines for the Care and Treatment for Breast Cancer: A Canadian Consensus Document. Guideline 4: Axillary Dissection. *Canadian Medical Association Journal* 1998; 158(3B): 22S-26S.

14. Carter CL, Allen C, Henson DE. Relation of tumour size, lymph node status, and survival in 24,740 breast cancer cases. *Cancer* 1989; 63: 181-187.
15. Recht A, Houlihan MJ. Axillary lymph nodes and breast cancer. *Cancer* 1995; 76: 1245-1248.
16. Brown RS, Wahl RL. Overexpression of Glut-1 Transporters in Human Breast Cancer. *Cancer* 1993; 72: 2979-2985.
17. Warburg O, Wind F, Neglers E. On the metabolism of tumours in the body. In: Warburg O, Ed. "Metabolism of tumours." London: Constable 1930;254-270.
18. Maffioli L, Seregni E, Nerini Molteni S, Massaron S, Crippa E, Bombardieri E. Breast cancer seeking agents: basic approach. *Quart J Nucl Med* 1997; 41: 211-224.
19. Karssemeijer N, Frieling J, Hendriks J. Spatial resolution in digital mammography. *Investigative Radiology* 1993; 28: 413-419.
20. Bird RE, Wallace TW, Yankaskas BC. Analysis of cancers missed at screening mammography. *Radiology* 1992; 184: 613-617.
21. Baker LH. Breast cancer detection demonstration project: 5 year summary report. *Cancer* 1992; 32: 194-225.
22. Yaffe MJ, Jennings RJ, Fahrig R, Fewell TR. X-ray Spectral Considerations for Mammography. *RSNA Categorical Course in Physics* 1994; 63-73.
23. Tabar L, Dean P. Mammographic parenchymal patterns: Risk indicator for breast cancer ? *Journal of the American Medical Association* 1982; 247: 185-189.
24. Säbel M, Aichinger H. Recent developments in breast imaging. *Phys. Med. Biol.* 1996; 41: 315-368.
25. Montanari G, Croce P, Zinzalini G, Mancastroppa A, Bertolotti PA. Echography in the diagnosis of breast cancer. *Minerva Chirurgica* 1991; 46: 845-848.
26. Cilotti A, Bagnelosi P, Moretti M, et al. Comparison of the diagnostic performance of high-frequency ultrasound as a first or second line diagnostic tool in non-palpable lesions of the breast. *European Radiology* 1997;7 :1240-1244.
27. Adler DD, Wahl RL. New methods for imaging the breast: techniques, findings, and potential. *American Journal of Roentgenology* 1995; 164:19-30.
28. Harms SE, Flamig DP. MR imaging of the breast. *J Magn Res Imaging* 1993; 3: 277-283.

29. Harms SE, Flamig DP, Hesley KL, et al. Fat-suppressed three-dimensional MR imaging of the breast. *Radiographics* 1993;131:247-267.
30. Heywang SH, Wolf A, Pruss E, et al. MR imaging of the breast with Gd-DTPA: use and limitations. *Radiology* 1989; 171: 95-103
31. Maubant J. Scintigraphic imaging of breast tumors. *Eur J of Radiology* 1997;24:2-10.
32. Khalkhali I, Mena I, Diggles L. Review of imaging techniques for the diagnosis of breast cancer: a new role for prone scintimammography using technetium-99m sestamibi. *Eur J Nucl Med* 1994; 21: 357-362.
33. Avril N, Bense S, Ziegler SI, et al. Breast Imaging with Fluorine-18-FDG-PET: Quantitative image analysis. *J Nucl Med* 1996;38:1186-1191
34. Thompson CJ, Murthy K, Weinberg IN, Mako F. Feasibility study for positron emission mammography. *Medical Physics* 1994; 21: 529-538.
35. Freifelder R, Karp JS. Dedicated PET scanners for breast imaging. *Physics in Medicine and Biology* 1997; 42: 2463-2480.
36. Sandell A, Erlandsson K, Bertenstam L. A scanner for positron emission mammography. In: Metabolic Imaging of Cancer - Proceedings of the European Conference on research and Application of PET in Oncology. Ed. Paans A, prium J, Franssen E, and Vaalburg W. Pages 88-89, PET-Centrum AZG, 1996.
37. Moses W, Budinger T, Huesman R, Derenzo S. PET camera designs for imaging breast cancer and axillary node involvement. *J Nucl Med* (abstract), 1995; 36:69P.
38. Worstell W, Johnson O, Zawarin V. Development of a high resolution PET detector using LSO and wavelength shifting fibers. *IEEE NSS/MIC conference record* 1995;3:1756-1760.
39. Weinberg I, Majewski S, Weisenberger A, et al. Preliminary results for positron emission tomography: real-time functional breast imaging in a conventional mammography gantry. *Eur J of Nucl Med* 1996; 23: 804-806.
40. Beck T. Dose tabulations for the clinical research committee of the Johns Hopkins Hospital [Baltimore MD]
41. Khalkhali I, Mena I, Diggles L. Review of imaging techniques for the diagnosis of breast cancer: a new role for prone scintimammography using technetium-99m sestamibi. *Eur J Nucl Med* 1994; 21: 357-362.
42. Anger HO. Patent entitled "Radiation Image Device". United States; patent No. 3,011,057 granted in 1961.

43. Gullberg GT, Budinger TF. The use of filtering methods to compensate for constant attenuation in single-photon emission computed tomography. *IEEE Trans. Biomed. Eng.* 1981; 28: 142-157.
44. Molison RT, Laruelle M, Innis RB. Positron and Single Emission Tomography. In: Psychopharmacology: the Fourth Generation of Progress. Ed. FE Bloom and DJ Kupfer, Paven Press Ltd., New York, 1995.
45. Cho ZH, Chan JK, Ericksson L, et al. Positron ranges obtained from biomedically important positron emitting radionuclides. *J Nucl Med* 1975;16:1174-2276
46. Benedetti SD, Cowan C, et al. On the angular distribution of two-photon annihilation radiation. *Physics Review*, 1950;77.
47. Figure adapted from: Bergman A. The evaluation of a Positron Emission Mammography System Using Images Co-registered with X-ray Mammograms. *Master's thesis, McGill University, Medical Physics Unit*, July 1997.
48. Johns EH, Cunningham JR. The Physics of Radiology fourth ed. Springfield: C. Thomas, 1983.
49. Hoffman EJ et al. Examination of the role of detection systems in quantitation and image quality in PET. *IEEE Transactions on Nuclear Science* 1986; 33: 420-424.
50. Ishibashi H. Cerium-doped GSO Scintillator and its applications to Position Sensitive detectors. *IEEE Transactions on Nuclear Science* 1989; 36: 170-172.
51. Melcher C, Schweitzer J. Cerium-doped lutetium oxyorthosilicate: A fast, efficient new scintillator. *IEEE Transactions on Nuclear Science* 1992; 39: 502-505.
52. Rigo P, Pauls P, Kaschten BJ, et al. Oncological applications of positron emission tomography with fluorine-18 fluorodeoxyglucose. *Eur J Nucl Med* 1996;12:1641-1674
53. Wahl RL, Cody RL, Hutchins GD, Mudgett EE. Primary and Metastatic Breast Carcinoma: Initial Clinical Evaluation with PET with the Radiolabeled Glucose Analogue 2-[F-18]-Fluoro-2-deoxy-D-glucose. *Radiology* 1991; 179:765-770.
54. Amano S, Inoue T, Tomiyoshi K, Ando T, Endo K. In Vivo Comparison of PET and SPECT Radiopharmaceuticals in Detecting Breast Cancer. *J Nucl Med* 1998;39:1424-1427.

55. Thompson CJ. Personal communication, March 1999.
56. Smith-Jones PM, Stolz B, Bruns C, et al. Gallium-67/Gallium-68-[DFO]-Octreotide: A potential radiopharmaceutical for PET imaging of Somatostatin receptor-positive tumours: Synthesis and radiolabeling in vitro and preliminary in vivo studies. *J Nucl Med* 1994; 35: 317-325.
57. Thompson CJ, Murthy K, Picard Y, Weinberg I, Mako R. Positron emission mammography (PEM): A promising technique for detecting breast cancer. *IEEE Transactions in Nuclear Science* 1995; 42: 1012-1017
58. Thompson CJ, Weinberg I, Mako F. Patent Entitled : "Dedicated Apparatus and Method for Emission Mammography." United States; patent No. 5,323,006 granted 21st June 1994.
59. Clancy R, Thompson C, Robar J, Bergman A. A simple technique to increase the linearity and field-of-view in position sensitive photomultiplier tubes. *IEEE Transactions on Nuclear Science* 1997; 44: 494-503.
60. Robar JL, Thompson CJ, Murthy K, Clancy RL, Bergman AL. Construction and calibration of detectors for high resolution metabolic breast cancer imaging. *Nucl. Inst. And Meth. A* 1997; 32: 402-406.
61. Bergman AM, Thompson CJ, Murthy K. Technique to obtain positron emission mammography images in registration with x-ray mammograms. *Medical Physics* 1998; 25: 2119-2129.
62. Shelbert HR, Hoh CK, Royal HD, Brown M, Dahlbom MN, Dehdashti F, Wahl RL. Procedure guideline for tumor imaging using fluorine-18-FDG. *J Nucl Med* 1998;39:1302-1305
63. Lindholm P, Minn H, Leskinen-Kallio S, et al. Influence of the blood glucose concentration on FDG uptake in cancer - a PET study. *J Nucl Med* 1993;34:1-6.
64. Sokoloff L, Reivich M, Kennedy C, et al. The [14-C]deoxyglucose method for the measurement of local cerebral glucose utilization: theory, procedure and normal values in the conscious and anesthetized albino rat. *J Neuro-chem* 1977; 28:897-916.
65. Phelps ME, Huang SC, Hoffman EJ, Selin C, Sokoloff L, Kuhl DE. Tomographic measurement of local cerebral glucose metabolic rate in humans with (F-18)2-Fluoro-2-Deoxy-D-Glucose: Validation of method. *Ann Neurol* 1979;6:371-388.

66. Kim CK, Gupta NC, Chandramouli B, Alavi A. Standardized Uptake Values of FDG: Body Surface Area Correction is Preferable to Body Weight Correction. *J Nucl Med* 1994; 35:164-167.
67. Zasadny KR, Wahl RL. Standardized Uptake Value of Normal Tissues at PET with 2-[Fluorine-18]-Fluoro-2-deoxy-D-glucose: Variations with Body Weight and a Method for Corrections. *Radiology* 1993; 189:847-850
68. Keyes JWJ. SUV: Standardized Uptake Value or Silly Useless Value ? *J Nucl Med* 1995; 36: 1836-1839.
69. Hamberg LM, Hunter GJ, Alpert NM, Choi NC, Babich JW, Fischman AJ. The Dose Uptake Ratio as an Index of Glucose Metabolism: Useful Parameter or Oversimplification? *J Nucl Med* 1994; 35: 1308-1312.
70. Fisher ER, Fisher B, sass R, Wickerham L. Pathologic findings from the National Surgical Adjuvant Breast Project (Protocol No. 4). XI. Bilateral Breast Cancer. *Cancer* 1984; 54: 3002-3011.
71. Wahl RL, Cody RL, Hutchins GD, Mudgett EE. Primary and Metastatic Breast Carcinoma: Initial Clinical Evaluation with PET with the Radiolabeled Glucose Analogue 2-[F-18]-Fluoro-2-deoxy-D-glucose. *Radiology* 1991; 179:765-770.
72. Huang SC, Phelps ME, Hoffman EJ, Sideris K, Selin CJ, Kuhl DE. Noninvasive determination of local cerebral metabolic rate of glucose in man. *Am J Physiol* 1980;238:E69-E82.
73. Metz CE. Basic Principles of ROC Analysis. *Seminars in Nuclear Medicine* 1978; 8:283-298.
74. Murthy K, Jolly D, Aznar M. Quantification in Positron Emission Mammography (PEM) with Planar Detectors: Contrast Resolution Measurements using a Custom Breast Phantom and Novel Spherical Hot-Spots. *Poster presented at IEEE conference, Toronto, November 1998.*
75. Sorenson JA, Phelps ME. Physics in Nuclear Medicine. 2nd ed. Philadelphia: WB Saunders Company, 1987. 252-259.
76. Gallagher BM, Ansari A, Atkins H et al. Radiopharmaceuticals XXVIII. 18F-Labeled 2-Deoxy-2-Fluoro-D-Glucose as a radiopharmaceutical for Measuring regional myocardial glucose metabolism in vivo: tissue distribution and imaging studies in animals. *J Nucl Med* 1997; 18:990-996.
77. Tortora GJ, Grabowski SR. Principles of Anatomy and Physiology eight ed. New York: Harper Collins College, 1996. 580-581.

78. Sokoloff L. The [14C]deoxyglucose method: four years later. *Acta Neurol Scand* 1979; 60(suppl 70): 640-649.

79. Hamberg LM, Hunter GJ, Fischman AJ. Use of positron emission tomography to study tumours in vivo. *Molecular Medicine Today* 1996;12:528-534.

80. Wahl RL, Zasadny K, Helvie M, et al. Metabolic monitoring of breast cancer chemohormonotherapy using positron emission tomography: initial evaluation. *J Clin Oncol* 1993;11:2101-2111.

81. Bruce DM, Evans NTS, Heys SD et al. Positron emission tomography: 2-deoxy-2-[18F]-fluoro-D-glucose uptake in locally advanced breast cancers. *European Journal of Surgical Oncology* 1995; 21:280-283.